CAST Proposal/Status report to the CERN SPSC for the 135th Meeting

CERN-SPSC-2019-038 / SPSC-SR-259
02/10/2019

CERN - October 15th, 2019

Editor: G. Cantatore (University and INFN Trieste)

Executive summary

Despite the compelling evidence for Dark Matter and Dark Energy it remains to identify their physical nature. CAST is redoubling its efforts to solve these long-standing puzzles, developing and installing different types of resonant high frequency cavities to search for dark matter axions (CAST-CAPP and RADES), a low background MicroMegas detector for solar axion search and an optomechanical sensor (KWISP) to detect chameleons by their interaction with matter. Chameleons have been postulated as possible Dark Energy candidates.
Parallel to data taking, CAST pursues a very aggressive R&D program to further improve the sensitivity of its detectors. This activity must also be seen in the face of the preparation of Baby-IAXO. Here CAST offers the priceless advantage to be also a host test facility for Baby-IAXO detectors.

Four CAPP cavities have been installed and all perform impeccably. We succeeded in running and taking first data with all cavities at an axion mass range around 22 μeV. We are confident that we can repeat soon phase matching also at 9 T. The present cavity temperature is high (>10K) due to warming by the amplifier, but we have various options to reduce the warming-up.
The fast resonance scanning mechanism was tested for the first time for a frequency range of 50 MHz around ~5.1 GHz and with 200 kHz steps. Presently, one single scan lasts ~2 hours. This method opens the window to detect DM axion streams or axion clusters, respectively, provided the axion mass and its flux are fitting-in. Figure 1shows CAST present results with 7 hours of data taken, projected future expectations and its new discovery potential. This scanning is a novel technique in DM research. Following Figure 1 the required axion flux enhancement for such a short time period even for QCD axions is relatively modest. Thus, if during the 7 hours run there was a stream of ~10^4× above the isotropic DM axion density, CAST could have detected it, provided the axion mass is within this mass range.
In addition, we are investigating an alternative wideband technique to scan the accessible axion mass range. The approach is based on out of resonance scanning, abandoning the resonance enhancement. This could also be compensated by an appropriate temporal axion flux enhancement. The minimum single scanning period achieved so far is ~10 minutes and is done automatically for several hours.
Furthermore, in parallel to the data taking, we are exploring to transform the present cavities to superconducting ones covering the inner cavity surface with superconducting tape. This has been successfully tested in Korea and reported at the PATRAS2019 workshop. With such an upgrade, CAST could become world leading with QCD axion discovery potential (see Figure 1).
Today, with CAST-CAPP we have a unique DM axion detector able to address more fundamental physics questions such as the search for axion bursts from Anti Quark Nuggets (AQNs). AQNs have been suggested to solve the DM problem, the matter-antimatter asymmetry, while providing possible explanation for other unsolved problems in outer space.

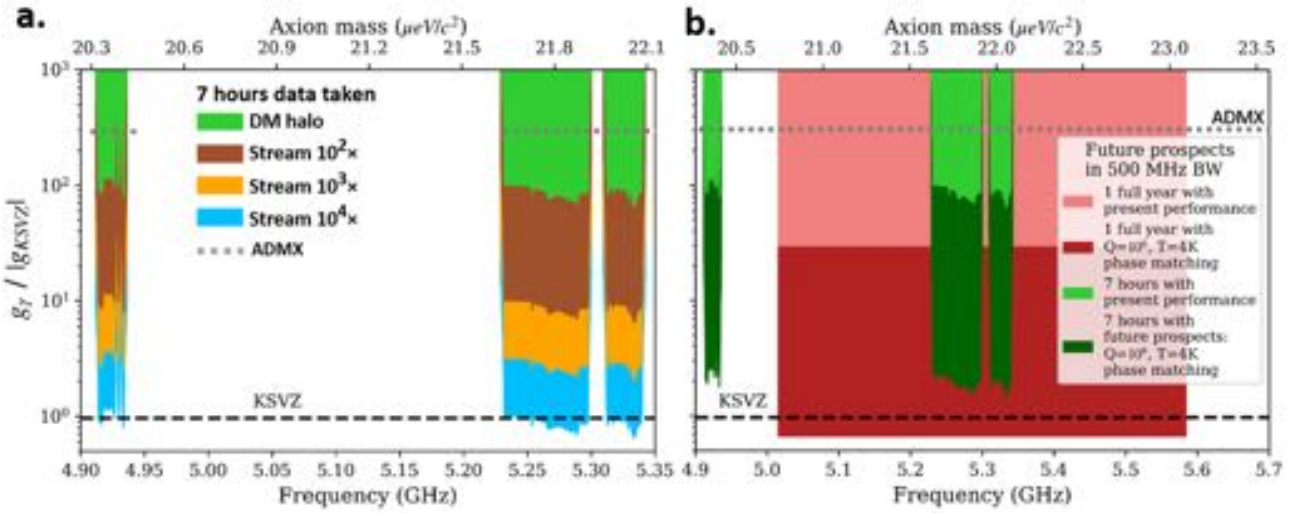

Figure 1: (a.) Exclusion plot tuning one CAPP cavity at a time assuming galactic halo DM axions and streaming DM axions. Measuring time ~7 hours. E.g., an axion signature could have been observed in case of an axion stream or axion cluster lasting for about 1 hour with a density ~104 × 0.3 GeV/cm3, and, for axions in this mass range with the theoretical coupling constant (KSVZ line). For comparison, it is given also the limit measured by ADMX. (b.) Perspectives for future longtime measurements assuming the present and improved cavity performance, e.g., Q=106 following recent R&D work [https://indico.desy.de/indico/event/22598/session/2/contribution/63/material/slides/0.pdf].

We are happy to emphasize that we succeeded in two major goals for 2019 for the RADES sub-detector. In 2019, we are taking data with a 30 sub-cavities alternating irises cavity of a length of approximately 1m. In the plot shown in Figure 2 we assume Q = 1200 (measured value), coupling β = 0.75 (measured value), at a central mass of 8.37 GHz and thus a mass of m = 34.62 μeV, a geometrical factor of G = 0.55 (simulated value) as well as a data taking time of around 3 months (12 weeks). From the plot of Figure 2, it is visible that the long alternating cavity is not much more sensitive than the short inductive. This is due to the low Q. However, on the long term, the volume is more important than the quality factor as the scanning speed for axions $\frac{df}{dt}\frac{f}{Q}$. This is why gaining volume in the prospect of tunable cavities is in principle more important than a large quality factor.
For 2020 we propose to install for the first time a cavity with tunable resonance frequency. A short cavity and its tuning mechanism are currently being tested at CERN's cryogenics laboratory to mitigate potential risks for 2020 data taking well ahead of time. Assumptions is a tuning range of 600 MHz achievable in the cold. With a width of ~3 MHz we might scan for 200 Steps in 24 weeks, i.e. ~ each 17 h for one scan step. We assume a conservative Q value of 6000 although this cavity type even higher Q values up to 10000 could be reached.
For the data taking in 2021 we will put emphasis on a 3 m long cavity. We have observed that machining a single piece cavity beyond the 1 m scale becomes unfeasible mechanically, thus we opt for a set of ~110 short sub-cavities that can be assembled flexibly for the bore length. With the modular concept, we have now a realistic approach towards increasing the length.
The RADES project has been conceived with the long-term goal of performing axion-dark-matter searches also with Baby-IAXO. The crucial work in preparing Baby-IAXO for a future haloscope data-taking with RADES cavities will be to foresee interfaces and connectors to accommodate the RADES tuning feedthroughs and validate the tuning principle. Regular meetings between the RADES group and the CERN Baby-IAXO magnet team are scheduled. The baseline schedule of Baby-IAXO foresees data taking ~2023 with vacuum and gas phases to search for solar axions. At a later stage, data taking with RADES-type cavities inside the Baby-IAXO magnet bore is considered for searches of relic axions. However, if solar tracking is delayed due to unforeseen problems during Baby-IAXO installations the RADES project might be rescheduled for commissioning in 2023.

The experience with CAST: live cryogenic, vibrating/sun-tracking environment with a strong magnetic field is unique and the development of expertise at CAST is mandatory to transition smoothly from solar data taking with Baby-IAXO to cavities. In conclusion, CAST is a unique opportunity to develop the needed experience in exploiting the full physics potential of Baby-IAXO.

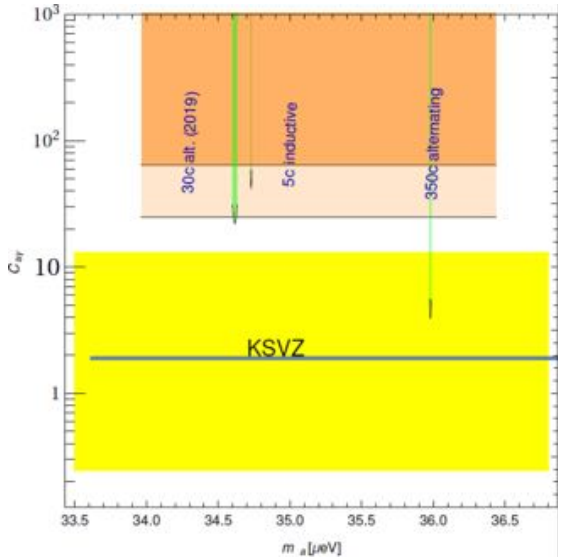

Figure 2 : Prospects of reach in the axion coupling-mass plane with RADES type cavities. The yellow band denotes typical axion models and the KSVZ model is denoted with a blue line, the ``5-c inductive'' line is a prospect of existing 2018 data upon finalization of the analysis. The ``30c alt." line is a prospect of the reach with this year's data (2019). The orange areas denote prospects for a hypothetical short (2020) and long (2021?) tunable cavity, respectively. The ``350c alternating'' is a prospect for a hypothetical very long cavity built from individual modules.

CAST can continue to pursue Axion Physics without new investments by including a solar axion search program with state-of-the-art Micromegas detectors combined with a dedicated X-ray telescope.

We propose to resume solar axion searches at the sunrise end of CAST with the IAXO pathfinder system, composed by the new LLNL X-ray telescope (XRT), with improved low-background and low-threshold gas detectors (both the microbulk and the GridPix Micromegas detectors). The goals of the proposal are to at least improve the result obtained in the 2013-15 phase on $g_{a\gamma}$, clarify the statistical/systematic origin of the 2□-excess observed in the sunrise Micromegas (SRMM) data set, get insight into the limitations of current detection parameters (background and threshold) in both microbulk and GridPix technologies, and provide technical and operational experience for the future Baby-IAXO and IAXO

We plan a new data-taking campaign targeting up to 20 months of effective exposure, which could presumably be accommodated in 3 annual campaigns, given that this activity does not conflict with CAST-CAPP and RADES runs. The total exposure time should be shared between the microbulk and the GridPix detectors. We aim to at least 13 months of data taking with similar or better detection parameters with respect to the ones enjoyed by the microbulk detector in 2015, in order to multiply ×3 the existing SRMM statistics. A time slot of 1-2 months could be reserved to test other detector technologies, interesting for Baby-IAXO. The exact periods for GridPix/microbulk would be determined later on by the proponent groups in accordance with the progress and improvement plans on the detectors.

The XRT, detectors and shielding are already installed in CAST and therefore this proposal does not rely on any important investment. The proponent groups need to find resources for maintenance and operation of the systems in CAST during the proposed period, shifts, etc. which seems feasible.

A number of technical improvements on the detectors are under consideration and are being carried out as part of the preparatory phase of IAXO. They include change of the detector gas to a Xenon mixture, instead of Argon, change to a self-triggered DAQ electronics based on the AGET chip, development of thinner and smaller x-ray windows, and larger area GridPix detectors with improved low-background capabilities.
CAST provides the closest conditions to the ones of Baby-IAXO, being thus the ideal platform to test those improvements, while the extensive and thorough data processing, necessary to achieve the very low background levels, will also include physics outcome.

In addition to Dark Matter and Axion Physics, CAST has also entered the quest to identify a possible Dark Energy candidate, chameleon fields being the most favored ones, with the GridPix photon detector and the KWISP force sensor.
The improved GridPix detector has taken two successful runs in 11/2017-03/2018 (Run2) and 10/2018-12/2018 (Run3). The improved detector, with respect to the Run1 unit, features six additional GridPix chips surrounding the central chip as veto detectors, as well as additional two veto scintillators and an FADC readout of the induced signal on the grid. While the six GridPix veto chips were available both for Run2 and Run3, scintillators and FADC were only usable during Run3. In addition, the detector features an ultra-thin Silicon Nitride X-ray window with significantly improved transparency at low energies with respect to the Run1 detector. X-ray calibration data have been taken in 02/2019.The full analysis of the data is still ongoing. Calibration data have been analyzed but are not yet fully applied to the analysis. The new analysis software qualitatively reproduces the results obtained on the central chip with the previous software but some differences at low energy remain and still have to be understood. The application of the new vetoes (6-GridPix veto, scintillator veto, FADC veto) has been implemented in a preliminary fashion. While scintillator and FADC veto only mildly reduces the background when applied to the „gold“ region, i.e. the most sensitive, central region of the chip with lowest background, preliminary analysis of the 6-GridPix veto shows a considerable background reduction, particularly at energies below ~2keV, i.e. in the energy range most relevant for solar Chameleon and axion-electron coupling searches. The full analysis is still ongoing with the goal to produce a publication on an improved solar Chameleon search and, depending on the final sensitivity, a further publication on an improved axion-electron coupling search. In parallel, an improved model of solar axion production and of the LLNL X-ray telescope optics has been coded and will be used in the final analysis Currently, no further data taking with the GridPix detector in CAST is planned

Results obtained with an initial version of the detector, dubbed KWISP 1.5, have been recently published in Physics of the Dark Universe. In a data taking campaign conducted in 2017, KWISP 1.5 reached a minimum detectable force level of 80 pN at 95% confidence level, allowing us to set original bounds in the chameleon parameter space β_γ-β_m (photon coupling – matter coupling).
KWISP version 3.0 is now running, where membrane displacements are sensed by a Fabry-Perot interferometer. The main features of KWISP 3.0 are complete fiber-optic beam transport, single-piece monolithic aluminum base, miniaturized optics and full passive vibration isolation. This last feature allows continuous operation of the sensor in the frequency-locked state also with vacuum pumping running. This was not possible with previous versions. In addition, the aluminum base makes it also ready to be integrated in a cryogenic cooling system designed to bring the temperature of the membrane down to 4 K or lower. The amplitude modulation of the incoming chameleon beam is now accomplished by a DLP chip consisting of about 4 million micro-mirrors which can be synchronously tilted, thus providing chopping action on the chameleon beam at a frequency of about 2.5 kHz. KWISP 3.0 aims at achieving shot-noise limited operation, which means detecting membrane displacements of the order of a femtometer. CAST is currently taking sun-tracking physics data with

KWISP 3.0 at an initial sensitivity of about $5 \cdot 10^{-14}$ m/√Hz, allowing us to reach a force limit of 2.4 pN in 554 s of integration time. This means that in about 8 days of data taking we can already improve the bound published with KWISP 1.5 by a factor 10.
In order to bring the room temperature sensitivity down to the shot noise level (a factor 10-50 below the current one) a series of improvements is planned for KWISP, among them upgrades in the mechanical design, in the optics layout, and homodyne readout of the interferometer signal. A further gain in sensitivity to a signal can be expected by lowering the membrane resonant frequency to match the chopper frequency. We are planning tests on sample membranes specially coated for this purpose. Higher frequency capable choppers are also becoming available, increasing the current upper chopper frequency limit (~10 kHz) by a factor 4.
A leap in sensitivity for KWISP will come by operating the sensor at cryogenic temperatures. We foresee starting in 2020 a feasibility study for a Liquid-He cryostat to bring the system down to 4 Kelvin, improving on the room temperature shot-noise sensitivity by a further factor of 10, for a total factor of up to 500-1000 with respect to the present one. If preliminary studies are successful, and funding becomes available, cryostat construction and operation can begin in 2021. The ultimate goal would be to achieve milli-Kelvin temperatures by equipping the LHe cryostat with a dilution refrigerator stage. In this regime the detector would be sensitive to attometer membrane displacements, comparable to the capability of present interferometric gravitational wave detectors. In this case, CAST would have the potential to reach a ~100 times better sensitivity in the chameleon parameter space.

After the installation of all the detectors, the CAST magnet was cooled down on the 2nd of September. Data taking with KWISP started on the 8th of September. The magnet "quench training" was completed on the 11th of September. The data taking with the MicroMegas detectors (solar tracking) and the cavities started, with the magnetic field ON, on the 12th of September.

Dark Matter Axion searches

CAST-CAPP performance

Yannis Semertzidis, Woohyun Chung, Caglar Kutlu, Soohyung Lee, SungWoo Youn, Fritz Caspers, Serkant Cetin, Horst Fischer, Wolfgang Funk, Antonios Gardikiotis, Marios Maroudas, Kaan Ozbozduman, Thodoros Vafeiadis, Manfred Wendt

Summary

Four cavities have been installed and all four perform impeccably. The last 2 weeks we have succeeded to perform far more than the envisaged pilot run, as we have achieved already some breakthroughs, allowing us to expect further improvements and aiming at new physics. Thus:
1. Since September 15th we succeeded to run and take data with all 4 cavities (B = 9 T, Q ~ 10^4) at an axion mass range around 22 μeV, which, other experiments, cannot cover easily in near future. Figure 17 shows CAST present results, projected future expectations and its new discovery potential [1].
2. The fast resonance scanning mechanism was tested for the first time for a frequency range of 50 MHz around ~5.1 GHz with 200 kHz steps. One single scan with 15 s per data-taking step lasts ~120 minutes. This opens the possibility to detect a short axion stream or axion cluster lasting about this time period, provided the axion mass and its flux are fitting-in. Figure 17 shows the derived exclusion plot using data taken by all 4 cavities (in total 7 hours). This is a "first" in DM axion research [1-4]. Following Figure 17 the required axion flux enhancement for QCD axions is modest compared to previously discussed enhancements [2-5] by factor up to $10^{5\text{-}11}$, for the case of axion MiniClusters or due to gravitational focusing effects like the Earth(Moon)=>Sun=>GalacticCenter around December 18th within 5.5o (see Figure 1).
3. An alternative wideband technique is being investigated, which is based on an out of resonance scanning, abandoning the resonance enhancement factor Q. This could be compensated by a temporal axion flux enhancement accordingly. The minimum single scanning period achieved so far is ~10 minutes for 300 MHz range and is done automatically for several hours.
4. Other issues: a) Phase matching has been performed with 3 cavities at room temperature We are confident that we can repeat this also at 9 T, b) The present cavity temperature is high (>10K) due to warming by the amplifier. First test to reduce the warming-up of the heating source is scheduled; other options are under consideration for the next shutdown.
5. Transform the present cavities to superconducting ones covering the inner cavity surface with superconducting tape; this has been successfully tested in Korea [6], and Figure 17 shows the importance of such an upgrade.
6. CAST CAPP is now a unique DM axion detector able to address more fundamental physics questions such as the search for axion bursts (a few seconds) [7] from Anti Quark Nuggets (AQNs). AQNs have been suggested to solve the DM problem, the matter-antimatter asymmetry, while providing possible explanation for other unsolved problems in outer space.

1.1 Introduction

In October 2018 we started with the actual commissioning of the CAST-CAPP detection system, and we managed to assemble all the DAQ hardware and create the necessary DAQ software with which we took and analyzed data. In between (May 2019) we had a pilot run with cavity #3 where we took 27 h of data at a fixed frequency for 260 min, while tuning (in one direction) in a frequency range of 240 MHz.
During the current data-taking period (since August 2019) we succeeded to have all 4 cavities fully working, and we have taken data at cryogenic temperatures and magnetic field (9 T) with fast resonance tuning up to 50 MHz in steps of 200 kHz (both directions) with the use of JPE piezo actuators (see paragraph 1.2.1 for more details). The current speed of data-taking with tuning for 50 MHz is about 2 hours considering also the amount of time spend for each data-taking step of 200 kHz (15 s). In the next days/weeks we plan to take data in a much broader frequency range (~200 MHz) and also with phase matched cavities.
The resonance scanning has been implemented in CAST, in order to be sensitive also to DM axion streams or axion clusters. In fact, a not relativistic streaming dark matter can get focused by the gravitational field of the sun towards the position of the Earth, because of the $1/(\text{velocity})^2$ dependence of the deflection angle (see Figure 1).

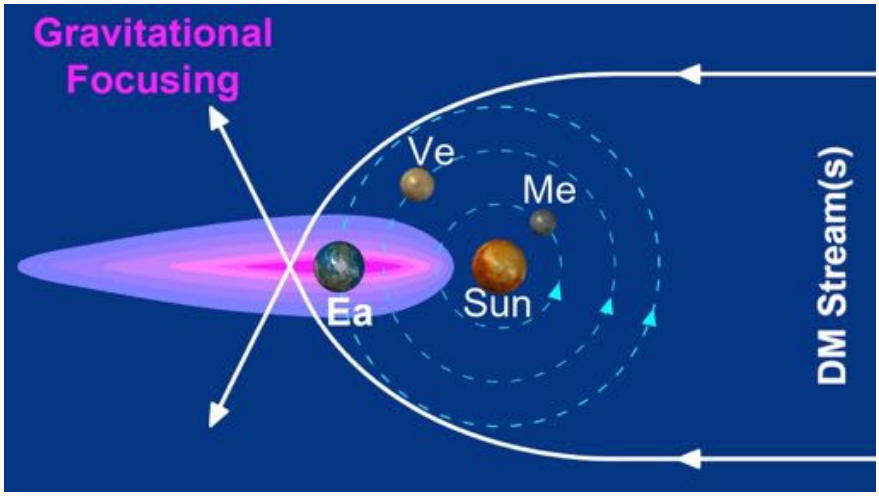

Figure 1: Schematic view of the flow of a putative slow stream. The sun can focus gravitationally streaming DM axions (and any other DM stream) very effectively, up to a factor of 10^{11}, while the stream is aligned with the Sun => Earth direction. E.g., in this specific Earth-Sun configuration around the 18th December, a putative axion DM stream could come (within 5.5°) from the direction of the Galactic Center.

In addition, we have also been investigating a new technique for a wide band scanning out of resonance which actually corresponds to a Q = 1, even though we measure with a cavity with a large Q. We do this simply by changing the center frequency of the SA (spectrum Analyzer), while keeping the resonant frequency of the cavity at a fixed position (no tuning). This method acts as a "plan B" and has been tested parasitically when the fast scanning method was not running. More precisely we took data with all 4 cavities in a frequency range of 300 MHz in ~10 MHz steps. The total range of 300 MHz can be scanned within ~10 min. The total time of the data taken so far is about 50 h (see paragraph 1.2.2 for more details).

1.2 Experimental Part

1.2.1 Fast Resonant Frequency Tuning

With CAST-CAPP we can search for conventional axions as any other experiment, but, in addition, we introduce for the first time in axion dark matter research the "fast resonant scanning technique". While we are searching by default for galactic axions as any other experiment does, with the fast scanning mechanism we are sensitive also to DM axion streams and axion clusters. More specifically, a quite wide axion mass range can be scanned within a time period of a few hours to take advantage of possible streaming dark matter (focused) towards the Earth. With the *GAIA* data releases stellar streams started to emerge and more are expected. Dark matter is assumed to follow to some degree normal matter. The 18th December of each year remains an interesting time window due to the alignment GalacticCenter=>Sun=>Earth. Also, axion Mini Clusters are of potential interest for bursts of dense axions fluxes (with a possible "duty cycle" of ~1%). The increase in the axion density due to the focusing by the sun is given in https://doi.org/10.1103/PhysRevD.98.043013 (see Section V. A.): an enhancement factor, in the ideal case up to $\sim 10^{11}$ (see Figure 1), more than compensates even for the loss of the quality factor Q enhancement in the second method (see paragraph 1.1.2.).
The current piezo performance in data-taking conditions, allows for a maximum scanning speed of 5 MHz/30 s, and therefore, the full tuning range of 400 MHz (cavities 1#, #2, and #3) can be scanned within ~1 hour for each cavity. Of course, the total time of tuning with data taking depends on the applied data-taking time for each step but this can be adjusted depending on the requirements. A first successful test of tuning with magnetic field ON was performed during the recent 2019 test run for a range of 240 MHz within 260 minutes (in one direction). During the current data-taking period we have already taken data while tuning in both directions with all 4 cavities. The currently applied data-taking time is 15 s per step but in the future, it could be reduced to 5-10 s per step. More specifically:

- Cavity #2 was tuned for 50 MHz frequency range within 2 h in steps of 200 kHz,
- Cavity #1 was tuned for 21 MHz frequency range in steps of 200 kHz,
- Cavity #3 and #4 were tuned for 10 MHz frequency range in steps of 200 kHz.

The step size has been reduced to 200 kHz to have a much higher sensitivity to axions (The ideal step size is on the order of the cavity frequency mode peak width ~ center frequency/quality factor). In addition, the optimal tuning range (without any observable issues with the piezos) that was determined in warm, is about 200-250 MHz for every cavity, and it will be reached gradually with all cavities within the next weeks. The maximum tuning range with the current configuration is about 500 MHz but the performance of the piezos is not guaranteed and thus this range will be tested only after there are sufficient data for the optimal tuning range. The actual optimum range values for each cavity as measured in warm temperatures before the installation on CAST magnet are the following:

- Cavity #1: 5.15 - 5.34 GHz
- Cavity #2: 5.14 - 5.39 GHz
- Cavity #3: 5.20 - 5.40 GHz
- Cavity #4: 4.80 - 5.00 GHz

Whereas the maximum tuning frequency range values as measured in warm temperatures are:

- Cavity #1: 5.130 - 5.502 GHz
- Cavity #2: 5.072 - 5.490 GHz
- Cavity #3: 5.028 - 5.500 GHz
- Cavity #4: 4.742 - 5.402 GHz
-

1.2.2 Wide Band Scanning

The RF receiver sensitivity is maximized at the cavity resonant frequency, but the sensitivity away from the resonance is decreased by the response of the approximately critically coupled cavity (towards receiver) in transmission (and weakly coupled at the test port) according to its center frequency and Q value, but it does not become zero. The power output of the axion to RF-photon conversion is proportional to the quality factor Q with a (Lorentzian) tail. Thus, far outside the cavity resonance, the power level is equivalent to a quality factor of Q = 1, limited only by the RF-chain bandwidth (BW) including the detection and recording system.
Thus, by changing the center frequency of the SA while keeping the resonant frequency of the cavity at a fixed position (no tuning) we are able to detect an enhanced streaming axion signal (see Figure 2). So, as a "plan B" without tuning the cavities by activating the piezos, we can use the 4 cavities with their resonant frequencies fixed in a position where the distance between them is maximum and detect such a strong signal in a total range of about 1 GHz, or, ~5 μeV at ~20-25 μeV.
The key point in this second method as to the first one is that the resonant frequency remains at a fixed position and we change the position of the 10 MHz window (span) of the SA which is moving automatically in steps of 10 MHz towards lower frequencies of the resonance; data-taking for each position of the 10 MHz steps can be as fast as even 1-2 s. The analog bandwidth of the signal transmission system is broadband (~1 GHz and more), but the signal acquisition is set to 10 MHz (although the instrument can accept 25 MHz in the FFT mode (VSA, a not normal SA = spectrum analyzer mode), but operating with 25 MHz would give a huge data flow that quickly fills up the digital recorder. The electronics readout of the microwave cavities is kept broad-band, limited only by the span of the spectrum analyzer that is used to read-out the data.
The transmissivity of the RF-chain system with real data-taking conditions with magnetic field and cryo temperatures has been now tested with Cavity #4 as shown in Figure 2. We have used multiple test signals (-50 dBm to -100 dBm) sent from the VNA, using various attenuators simulating possible enhanced axion DM flux, to measure the actual sensitivity of our RF-chain system. In this procedure we use only the range on the left of the resonant frequency (towards lower frequencies) as there are no more resonances there and the mismatch of the input frequency with the cavity resonance means that most of the power is reflected due to impedance mismatch. In Figure 2, the X axis shows the distance from axion-sensitive resonance mode. These data were taken with cavity 4 which has several more resonance modes on the left side of main mode. The overall decrease of the signal power as we get away from the mode frequency indicates less sensitivity for dark matter streams. We can conclude from the plot that for WBS, with 10 second measurements at each step, we are not sensitive to signals below -90 dBm strength.

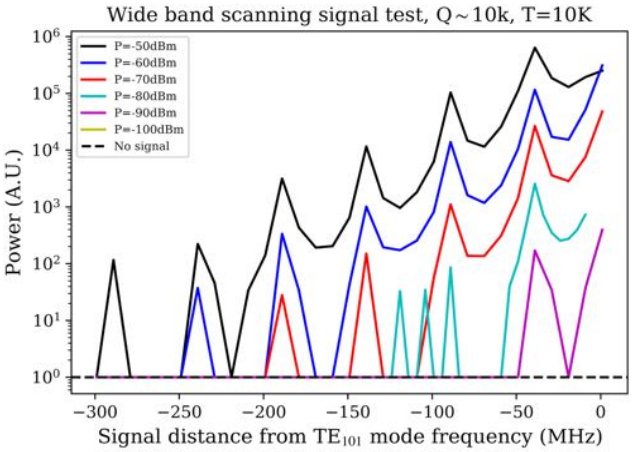

Figure 2: The measured power transmission *vs*. off the cavity resonance frequency.

During current data taking run we have measured with the wide band scanning technique for a total range of 300 MHz left of the resonant peak:

- With Cavity #2 in 5 MHz steps of 15 s for a total range of 300 MHz (1 loop)
- With Cavity #4 in 10 MHz steps of 10 s for a total range of 300 MHz (53 loops)
- With Cavity #3 in 10 MHz steps of 10 s for a total range of 300 MHz (40 loops)
- With Cavity #1 in 10 MHz steps of 10 s for a total range of 300 MHz (25 loops)

The amount of time required to scan the whole range of 300 MHz is currently about 10 min considering the data taking time for each step (10 MHz) but also the amount of time required by the DAQ software to run all the functions in order to set the correct parameters to the instruments. Each loop corresponds to a full scan of 300 MHz with the SA by moving backward and forward in order to arrive to the same starting position of the resonant frequency of the used cavity.

1.2.3 Future prospects

The quality factor Q of each cavity can be increased up to ~10^6 utilizing the new discovery in IBS/CAPP-Korea [4] that the HTS cavities using YBCO tape (see Figure 3) keeps its superconducting phase even at 8 T (the highest B-field available during the test), and increase the cavity volume to xyz *l*, by phase matching all the cavities. The development of the superconducting cavity, by attaching HTS tape on the cavity inner surface, will take at least half a year before it can be implemented.

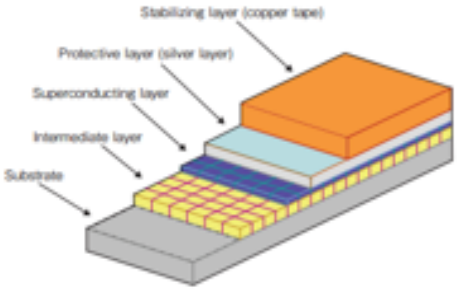

Figure 3**:** Structure of YBCO tape [6]

1.3 Hardware activities

All of the hardware issues mentioned in paragraph 1.2 of the SPSC report in 02/04/2019 have been addressed successfully. The ones remaining for the next installation is the replacement of the feedthroughs in the flanges, the full repair of the one corrupted RAID in IQC-Mem hardware and a possible enhancement of the piezos using better springs (see Figure 4 right).

1.3.1 Vibration damping

The vibration damping mechanism introduced, that consisted of 2 quartz glass tubes filled with Teflon foils and glued on the middle of the sapphire tuning strips, so as not to reduce the overall tuning range, (see Figure 4 Left) was tested in data taking conditions with cavity #3 that was installed on the magnet during 2019 test run. The idea is that the introduced friction of the Teflon foils touching the side walls of the cavity are reducing the vibration. Indeed, the vibration induced from CAST He pumps has been reduced significantly and thus the vibration damping technique was also installed in cavity #1. Due to the added force, the additional force required by the stepper motor in cryogenic

temperatures and the added friction from the vibration dampers, a fine tuning of the length of the Teflon and the quartz glass tubes is required. This was done for both cavities #1 and #3. This is the reason that it was not introduced to cavity #4, the sapphire tuning plates of which were repaired with UV glue (see paragraph 2.13 in SPSC report 06/2019). Cavity #2 was not opened at all to reduce the probability of an induced mechanical damage. As measured in cryogenic temperatures the vibrations in cavities #1 and #3 have been reduced but not in all frequency ranges. For example, for cavity #1, in frequencies near the upper limit of the overall tuning range, the vibration is getting worse. However, cavity #2 and #4 currently have very small vibrations which do not affect the data-taking procedure.

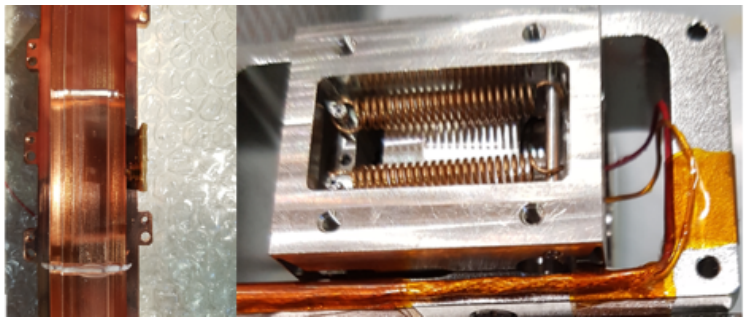

Figure 4**:** Vibration dampers on cavity #3 made of quartz glass tubes filled with Teflon (Left) and the 2 springs on the JPE piezo (Right).

1.3.2 Temperature Sensors

All temperature sensors have been restored successfully, and new ones have also been inserted. In the current installation we have 4 Temperatures in place (1 in cavity #1, 2 in cavity #2 and 1 in cavity #4). See paragraph 1.3.2 for the actual measurements while cooling down the magnet and while taking data. In the next installation we plan to install a temperature sensor also in cavity #3.

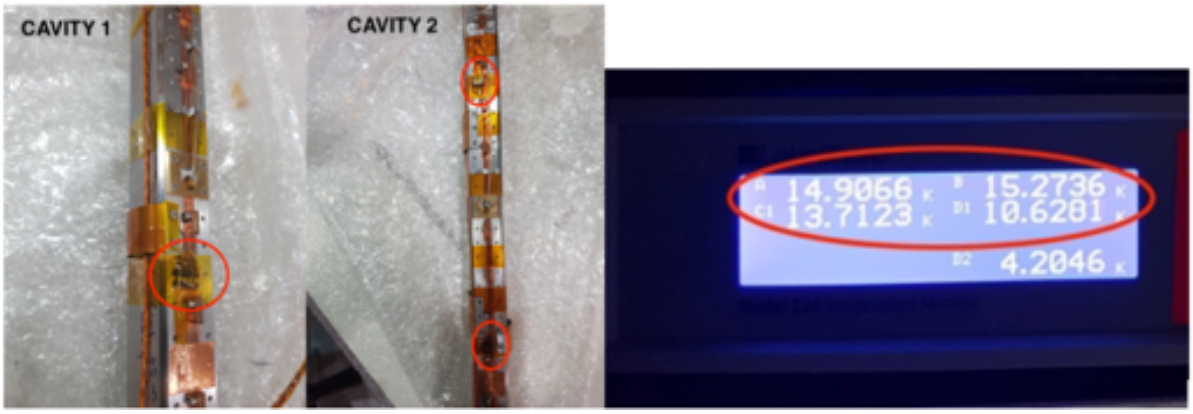

Figure 5: 1 Temperature Sensor in the middle of cavity #1 (Left) and 2 Temperature Sensors on the front and back side of cavity #2 (Middle). Screen on Lakeshore T-Monitor showing that all 4 T-sensors are working (Right).

1.3.3 New cabling and connectors

All RF copper cables of all cavities have been replaced with new continuous 0.047 malleable/sucoform cables from Novitronic AG company, to eliminate the many losses appearing in reflection due to intermediate connectors in the old cables (see paragraph 1.3.2 on the previous SPSC

report 02/04/2019). These new cables with the corresponding SMA and G3PO connectors have been assembled, connected and tested without any problem.

Figure 6: Old 0.047in RF cables with intermediate connectors (Left) and new 0.047in RF malleable/sucoform continuous cables (Right).

The DC connectors for the amplifiers of cavity #1 and cavity #2, that were damaged during previous installations were replaced and both amplifiers were tested and working as expected. More DC and RF connectors have been also acquired for redundancy for future repairs and installations.

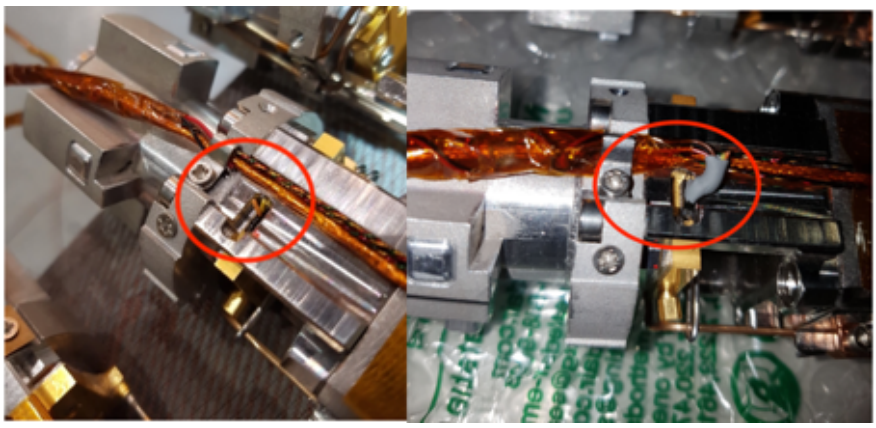

Figure 7: Cable of DC connector to amplifier which was previously cut (Left) has now been replaced with a new one (Right).

1.3.4 Antennas configurations

All the input and output antennas (Figure 8) have been replaced with new 0.047 RF cables and soldered again to existing brass plates, while measuring at room temperature the reflections around resonance with the VNA in Logmag, Phase and Smith charts (Figure 9), in order to achieve the correct under-critical coupling which eventually became near-critical in cryogenic temperatures.

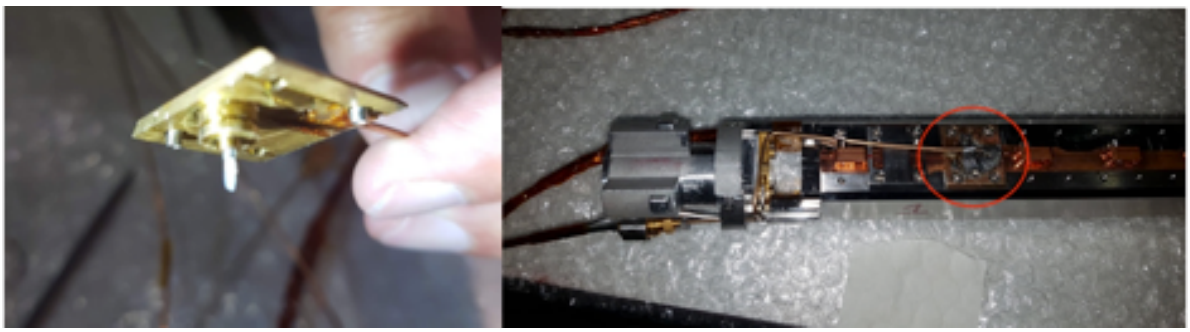

Figure 8: An example of a reconfigured antenna on a cavity.

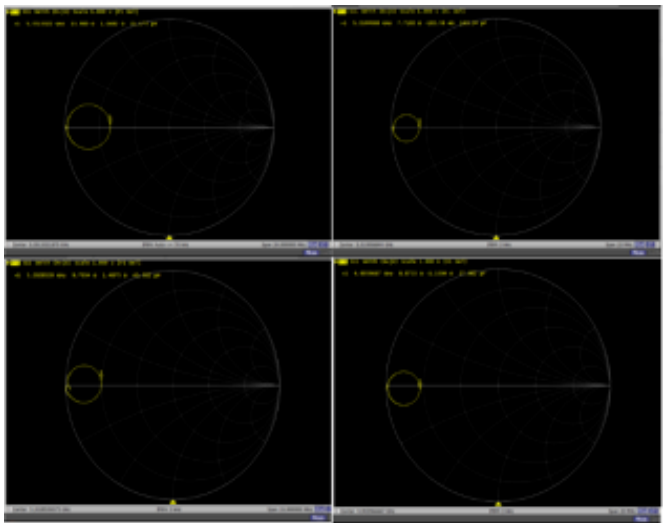

Figure 9: Output antenna reflections around Resonance in Smith Chart at Room temperatures for cavities #1 (Up Left), #2 (Up Right), #3 (Bottom Left), and #4 (Bottom Right).

1.3.5 Cable routing and cavities connection

The 4 cavities were connected all together using customized inox non-magnetic metal sheet and were then inserted together inside the magnet bore. In this way, all the cables could be attached on the sides of the cavities without any additional dangerous movement during the insertion of each cavity. This configuration facilitates the installation and extraction of the cavities and allows us to have a much higher accuracy for the alignment of all cavities with the magnetic field, as the cavities cannot rotate differentially but can bend in tandem to account for the curvature of the magnet bore. On the back side the empty "vacuum vessel" was inserted and locked on the magnet bore; on the front side cavity #4 was also locked on the magnet bore making the whole structure safe and stable during magnet movements and possible quenches. An 8mm endoscopic HD LED camera has also been acquired and positioned on the cavities extraction tool which enabled a close monitoring of the whole installation procedure to ensure the orientation of the cavities as well as the positioning of the cables inside the magnet bore.

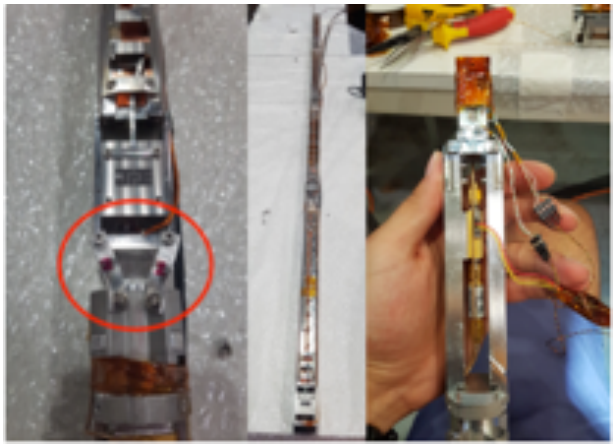

Figure 10: The metal-sheet parts that were created and installed to connect the 4 cavities together (Left) and all the 4 connected cavities before they were installed in the magnet (Middle). The "vacuum vessel" whose all electronic and RF components have been removed and has been inserted and locked on the back side of the cavities inside the magnet bore (Right).

1.3.6 Other

Two new RF Switches and 4 new external RF amplifiers (connected just after the output RF switch) have been acquired, tested and connected on the input and output lines of the cavities, in order to be able to switch automatically between the 4 cavities for data taking and measurements. A power combiner has also been inserted in the output line after the external amplifiers in order to account for phase matching between all 4 cavities. With this configuration, we can switch, measure and take data with single or multiple cavities at the same time without any hardware modification. An additional external amplifier has also been connected after the power combiner to account for all the added losses from the various intermediate cables, in order to achieve on the input of our instruments a signal difference of more than 10 dB between signal ON/OFF. Furthermore, a new web camera has been installed to monitor continuously the bias (voltage and current) of the power supplies of the internal low noise amplifiers of all 4 cavities. Finally, a new 1.98 kWatt APC UPS has been acquired and installed, with all sensitive CAPP instruments connected to it, to avoid any damage from voltage spikes, voltage dips, fluctuations and complete power failures caused by either quenches or the actual power lines. The new schematic of the CAPP DAQ chain with all the new instruments and connections is shown in Figure 11.

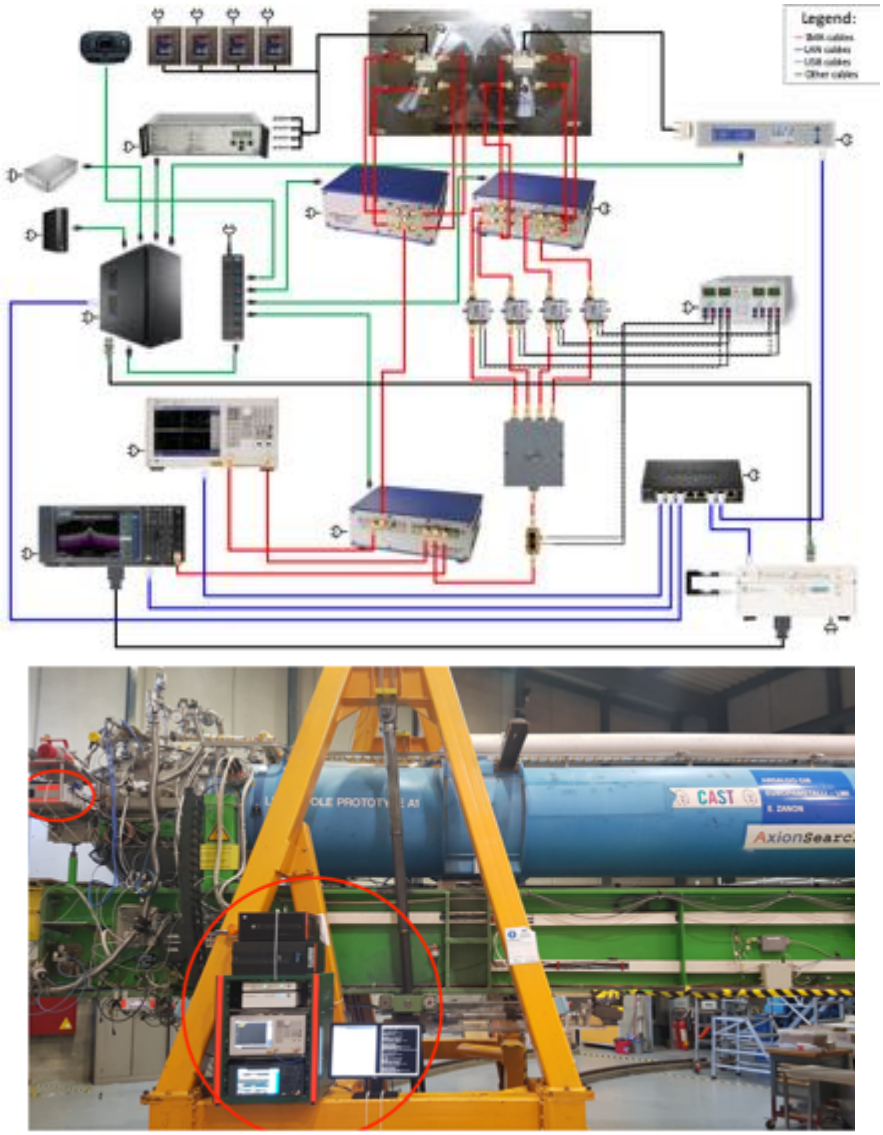

Figure 11: Hardware connection schematic (Top) and actual location of the various instruments on CAST (Bottom)

1.4 Measurements

1.4.1 Phase Matching

Phase matching of 3 cavities has already been achieved with a precision of 2° at warm temperature on 10/2018. All electrical signal path lengths have been adjusted within 1mm. In the next few days/weeks phase matching for cavities #1, #2 and #3 will also be performed again but in cold temperatures and data will also be taken as all hardware modifications for simultaneous measurements with all cavities have already been made (software modifications are ongoing). More specifically, 2 new RF switches, 4 new external low noise amplifiers and a power combiner have all been tested successfully and connected the DAQ chain system (see Figure 11 and Fig 12).

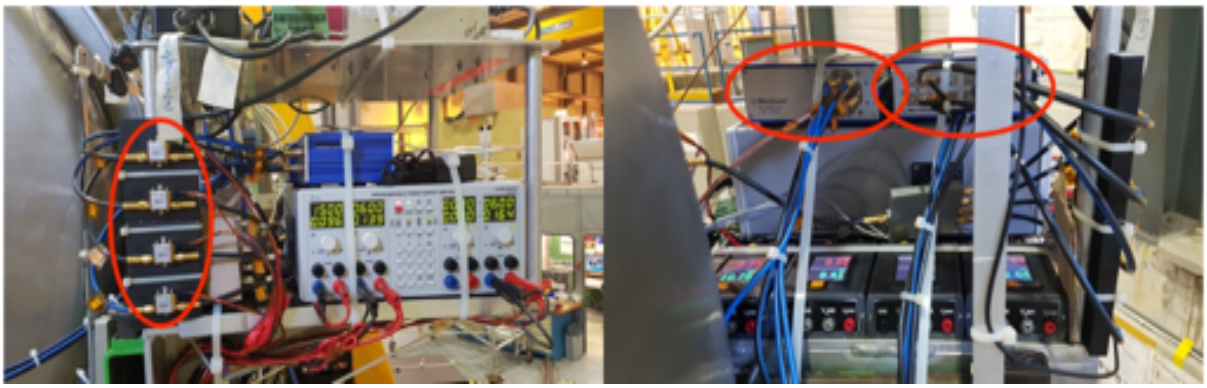

Figure 12: External pre-amplifiers (Left) and the 2 new RF Switches connected to the input and output of the cavities (Right).

1.4.2 Physical Temperature of the cavities

Using the temperature sensors mentioned in section 2.1.2, the temperature of the 4 cavities is measured continuously. The lower temperature of cavity #4 (yellow line) comparing to the other cavities is due to the better thermal conductivity through the anchors in the locking mechanism, which are touching the magnet bore. In future installation we will try to improve the thermal conductivity also for the rest of cavities. From these measurements we have calculated that the temperature difference between amplifiers ON/OFF is about 8-9 K. The current temperature of the 4 cavities in stable data taking conditions with the amplifiers continuously ON, is about 10-14 K. However, as confirmed by the company, this heat dissipation of 7.15 mW from the amplifiers can be reduced to 1.5 mW if the bias of the amplifiers by the power supplies is changed (from Vds = 0.55V to Vds = 0.25V) without a big sacrifice in noise. This will be tested in the next days. Furthermore, there is also some small heat dissipation (~0.3 K) from the movement of the piezos, but without any big effect on the temperatures recorded while taking data. The spikes observed in the temperature sensor of cavity #1 are artificial due to electronics discharging. The temperature measurements for each cavity are recorded before and after each data-taking step and the average is used for the analysis. For cavity #3 the average between cavity #2 and cavity #4 is used.

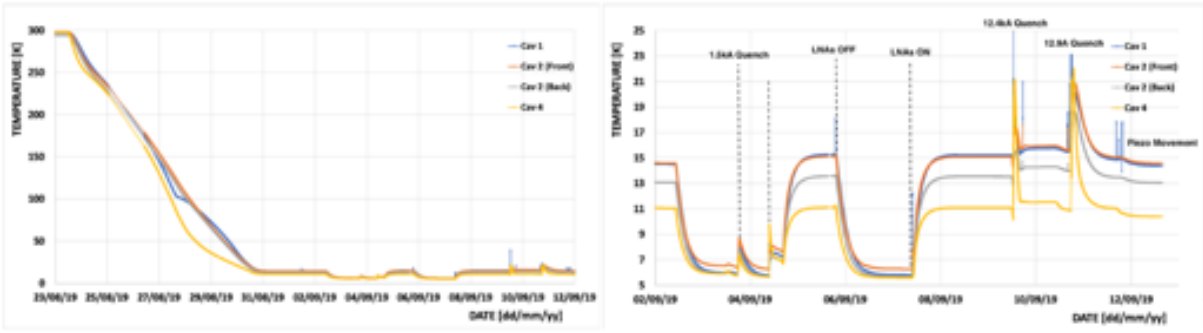

Figure 13: Temperature evolution during magnet cooldown (left) and during quench tests and amplifiers ON/OFF (Right)

1.4.3 S11 reflection measurements using VNA with time domain option

During the 05/2019 test run, Various S11 reflection measurements have been made using a VNA with time domain option to calculate the total attenuation from the output of the VNA until the input port of the cavity for T_{magnet} = 242 K. The reason of measuring the input cable is that on the output cable the LNA is in between thus making this measurement impossible without an RF switch or something similar for direct access to the output port of the cavity. By using the "Lowpass Impulse" (Figure 14A) and "Lowpass Step" (Figure 14B) mode in a VNA with time domain, we can find where the reflection from the cavity itself is located on the spectrum (marker Nr 6) and then by using the "Bandpass Impulse" (Figure 14C) mode (after setting the frequency to 4-7 GHz) we can measure the attenuation of all the cables all the way to the cavity. From that, we notice the power level of marker 6 is at ~ -70 dB, which means that the two-way attenuation from the end cable connecting to our instrument until the cavity is -70 dB; thus, the one-way attenuation is -35 dB. The same procedure has been done with a measurement directly from the warm flange instead of the end cable connecting to the VNA (not shown). In this measurement we found a total two-way attenuation of ~ -50 dB which means -25 dB one-way attenuation. Therefore, the cables until the warm flange have an attenuation of about -10 dB and the rest of the cables inside the magnet, copper vessel, and the magnet bores all the way to cavity itself have an attenuation of -25 dB. Furthermore, in Figure 14A, all the peaks, with the reflections that appear on the time domain spectrum, are due to intermediate connectors. Finally, one more information that we can get (Figure 14B) is that from marker 1 up to marker 3 are the long cables outside the magnet going from the VNA input all the way to the warm flange; from marker 3 up to marker 6 we see losses which are created by the new blue RF cables (see paragraph 1.1.6 on SPSC report on 02/04/2019) connecting the warm flange with the cold flange inside the magnet (these losses do not create any issue). The same measurements have been done on the warm flange input using a calibration kit for a "cleaner" spectrum, with no actual differences (not shown). Finally, with the same technique the same measurements have been done at the end cable connecting to the VNA input but during current data-taking period in cryogenic temperature with 9T magnetic field and a one-way attenuation of -24.9 dB, -24.6 dB, -23.7 dB, -21.3 dB has been calculated for cavities #1, #2, #3 and #4 accordingly.

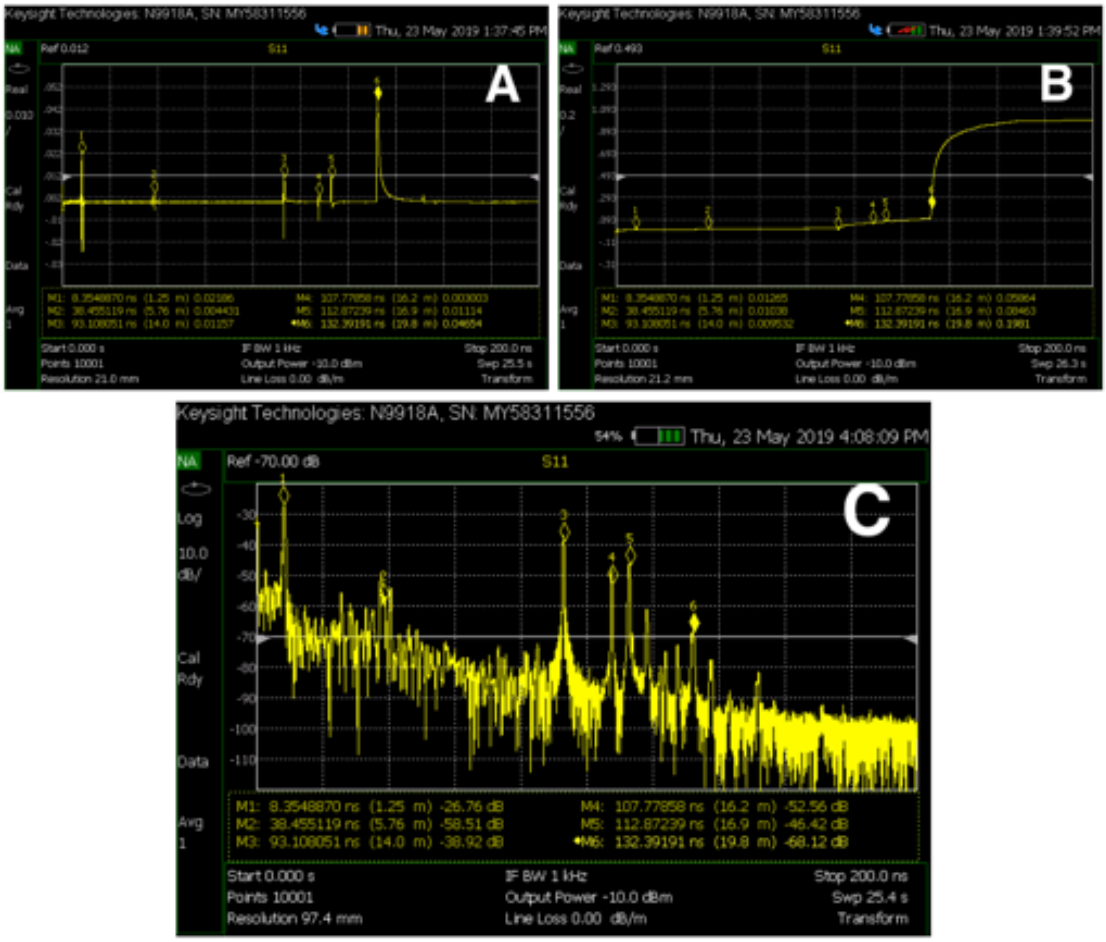

Figure 14: (A) Cavity #3 S11 measurement in "Time Lowpass Impulse" mode without CAL at the end cable connecting from the input of the VNA to the cavity for T_{magnet} = 242K. (B) Cavity #3 S11 measurement in "Time Lowpass Step" mode without CAL at the end cable for T_{magnet} = 242 K. (C) Cavity #3 S11 measurement in "Time Bandpass Impulse" mode without calibration for T_{magnet} = 242 K.

1.4.4 Noise Temperature as a function of B

Using the VNA as a signal generator we performed some noise figure measurements during 2019 test run for Cavity 3, via the 3 dB signal generator (twice power method) as a function of the CAST magnet current, which of course is analogous to the Magnetic Field (B). The measurements have been performed at the positions where the current was at one of the plateau in order to have an exact measurement. For these set of measurements, an RBW of 100kHz has been used along with a VBW of 1 Hz and span = 0 Hz. Note that also the resonant frequency of the cavity was changing during ramp up shifting towards lower frequencies for about 4 MHz (for comparison reasons, during ramp down the resonant peak shifts towards higher frequencies for about 0.1-0.3 M Hz) and this has been considered for every single measurement. By considering the total attenuation to the input of the cavity (see paragraph: 1.3.3) the noise temperature can be easily calculated the same way as it was done in paragraph 1.3.4 in the SPSC report of 30/01/2019. The same measurements have been done during current data-taking period in cryogenic temperatures for cavities #1, #2, #3 and #4 and a signal of -97 dBm, -95 dBm, -96 dBm, -81 dBm accordingly was required in order to have a 3 dB difference between signal ON/OFF. Therefore, our system noise temperature for the specific conditions of each cavity can be calculated to be about 14 K, 14 K, 4 K and 14 K for cavities #1, #2, #3 and #4 accordingly. These numbers have been inserted in the calculations for the exclusion plots (see below). An alternative method for the calculation of the noise temperature which will soon be tested is to alternate the bias voltage of the LNAs which gives us a known variation of the noise temperature and gain of the amplifier. Then from this variation of the bias we can measure in situ with the SA the

variation of the noise baseline (outside resonance) and make an estimation of the actual noise temperature of the system.

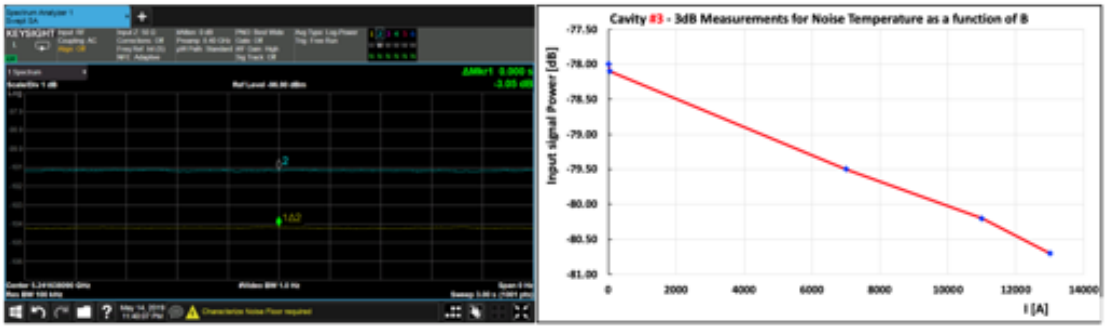

Figure 15: An example measurement for the maximum 13kA magnet current with an input of -80.7dBm (Left) and the plot with the various measurements for different currents (Right).

1.4.5 Noise Temperature as a function of T_{magnet}

The same measurements as in paragraph 1.3.4 have been performed during the 05/2019 test run, as function of the magnet temperature. The only difference between these measurements is the current (Id) and voltage (Vd) applied to the LNA of Cavity #3 which were changed depending on the temperature considering the nominal bias for 5 K and 296 K temperatures provided by the manufacturers and making a linear interpolation for all the intermediate values. Finally, as with the magnetic field, while the temperature of the cavity is decreasing, the resonant frequency of the cavity is also changing shifting towards lower frequencies.

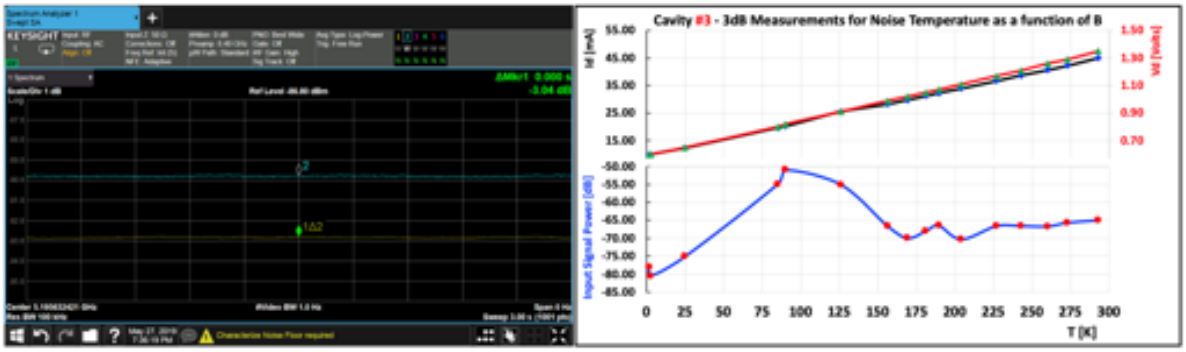

Figure 16: An example measurement for T_{magnet} = 293 K with an input of -65 dBm and Vd = 1.35 V, Id = 45 mA (Left) the plot with the various measurements for all different temperatures (Right).

1.5 DAQ system and data analysis

1.5.1 DAQ system

Data improved acquisition system allows to connect all programmable instruments (see Figure 11) in the setup and perform automatic operations which enables hands free data acquisition. DAQ controlled instruments: 1) Spectrum Analyzer (N9030B), 2) Vector Network Analyzer (E5063A), 3) IQC5000 data recorder, 4) Lakeshore 224 Temperature monitor, 5) JPE piezo controller and 6) 3 different Mini-circuits RF switches. The purpose of each instrument is the following:

- Python 32-bit based DAQ program employs IQC data recorder to connect to and record data from the spectrum analyser (SA).
- The Vector Network Analyzer (VNA) is used to measure the cavity mode frequency and quality factor through a transmission measurement before and after each data-taking measurement. VNA also acts as a fake signal source when needed. Automatic noise temperature measurement with VNA using the twice power method is also being developed.
- Lakeshore Temperature monitor currently monitors 4 temperature sensors (see paragraph 1.3.2. and 1.4.2) for CAPP. Before and after each measurement, the temperature of each cavity is read by all of these sensors.
- JPE piezo is connected to 4 piezo motors each one connected to 1 of the 4 cavities. These motors are controlled independently by DAQ and can be moved to any positions automatically, but they can of course be operated also manually when/if needed.
- 1SP4T RF switch (called “input switch”) is connected to the input cables of each cavity and directs the signal sent from VNA for transmission measurements to either one (only one) of the cavities.
- 4SPDT RF switch (called “output switch”) regulates the connection between output cables and the data processing instruments (SA or VNA) through external amplifiers (manually controlled out of necessity). This switch can actually connect any combination of cavity outputs to SA which allows us to acquire data from single or even multiple cavities by phase matching.
- 2SPDT switch (called “device switch”) connects accordingly the cavity input and/or output cables to the desired instruments (currently SA and VNA).

1.5.2 CERN CASTOR Storage

Post-data-acquisition processes (data offload and upload to CASTOR, analysis) are also being implemented in DAQ code to have a complete control software. More specifically, collaboration with IT department for automatic upload of the data-taking files to CASTOR through an automatic submission of json files from lxplus is currently under works. Currently the uploading procedure of the files through a dedicated service account (castcapp) has been accelerated but is still semi-manual due to difficulties with Windows OS. However, in the near future this will eventually be integrated on the DAQ program and be executed automatically at the end of each data-taking day.

1.5.3 Data taking in DAQ system

Currently, we use two different methods to acquire data. First is the standard data-taking with piezo driven tuning (see section 1.2.1). This procedure consists of serial (and separate) steps of data-taking and tuning. This technique is realized with automatic tuning for a step size down to 0.2 MHz which is close to the accepted standards (The ideal step size is on the order of the cavity frequency mode peak width ~ center frequency / quality factor). We currently take data for 15 seconds at each step. Since we can tune quite fast, it takes approximately 0.5 hours to scan 10 MHz range with a sensitivity one order of magnitude lower than the required, to reach KSVZ limit. With automatic tuning we have a potential to scan ~200 MHz range (limited by manually induced piezo tuner safety factors). More security measures are being introduced in the software to be able to run tuning measurements (where piezo driver has a chance to get stuck) without anybody watching the process.
The second technique is the so-called wide band scanning (WBS) where the cavity resonance mode frequency is kept fixed and the spectrum analyzer window is shifted on frequency axis (see section 1.2.2). This change in spectrum analyzer center frequency is needed as the limited acquisition bandwidth (span) of the instrument (15 MHz). WBS technique can be utilized for DM axion stream detection. Axion streams are predicted to have a burst like property, meaning that they will increase the local axion density by a significant amount (up to 11 orders of magnitude). In order to increase the chances to catch such a signal WBS measurements are kept very short (<=10 seconds) and a wide frequency range up to 300 MHz is scanned very fast (20 minutes back and forth). Moreover, at present, WBS measurements can be run overnight securely as they involve no piezo tuning. We have a potential to record approximately 2 TB data per day with WBS technique.

1.5.4 Data Analysis

The power from the axion conversion to microwave photons using the Sikivie method is given by

$$P = \left[\frac{\alpha g_\gamma}{\pi f_a}\right]^2 V B_0^2 \rho_a C m_a^{-1} Q_L$$

$$= 1 \times 10^{-23}\ \text{Watt} \left[\frac{V}{5\ \text{liter}}\right]\left[\frac{B_0}{7\ \text{Tesla}}\right]^2 \left[\frac{C}{0.4}\right]$$

$$\times \left[\frac{g_\gamma}{0.36}\right]^2 \left[\frac{\rho_a}{5\times10^{-25}\ \text{gr/cm}^3}\right]\left[\frac{m_a c^2}{\nu_a\ 5\ \text{GHz}}\right]\left[\frac{Q_L}{10^5}\right] \qquad (1)$$

Using the Dicke's radiometer equation

$$\frac{s}{n} = \frac{P}{kT_{sys}}\sqrt{\frac{t}{\Delta\nu}}$$

the scanning rate of the axion frequency results to be

$$\frac{df}{dt} = \frac{f}{Q}\frac{1}{t} \approx \frac{1\ \text{GHz}}{\text{year}}\left(g_{a\gamma\gamma}\ 10^{15}\ \text{GeV}\right)^4 \left[\frac{5\ \text{GHz}}{\nu_a}\right]^2 \left[\frac{4}{SNR}\right]^2 \left[\frac{0.25\ \text{K}}{T}\right]^2$$

$$\times \left[\frac{B}{25\ \text{T}}\right]^4 \left[\frac{c}{0.6}\right]^2 \left[\frac{V}{5\ l}\right]^2 \left[\frac{Q}{10^5}\right] \qquad (2)$$

which, assuming we could reach the stated parameter values, means that we could scan quite a large axion frequency range per year. However, for $B = 9$ T, $T = 4$ K, $V = xyz\ l$, and $Q = 2\times10^5$, it is hard to reach the hadronic axion sensitivity within reasonable time. As already mentioned, to mitigate the situation, we have commissioned taken data and analyzed them with 2 different methods (see sections 1.2.1, 1.2.2 and 1.5.3) which bring us at an advantageous position regarding the other axion dark matter activities around the world.
More specifically the analysis of the 2019 auto-tuning data is made up to more than 1500 15-s data files totaling 6 hours (cavity 2). The rest of the measurements (4 hours with other cavities) are being

handled. Data processing and analysis software are adapted to the auto-tuning measurements. Data analysis time increases exponentially with increasing number of data files and widening total frequency range. We will adopt a new approach for analysis, not to combine all files in the beginning: We will divide them into sub-groups, analyze each group separately and combined the results at last step. For now, this approach is being introduced and tested.
Currently analyzed dataset spans 50 MHz bandwidth at ~5.28 GHz (see Figure 17). The main scheme of this analysis is adapted from the HAYSTAC axion search procedure, which consists of scaling each spectrum (obtained from each data file) with respect to the expected conversion power of KSVZ axion in the presence of thermal noise. In detail, all datafiles are divided into chunks of 100 kBytes (total bandwidth/resolution bandwidth). Each chunk is applied fast Fourier transform (FFT) then combined together to have a processed spectrum out of one data file. Processed spectra are scaled according to the center frequency of the measurement and the quality factor. And the scaled spectra are combined with weighted averaging optimized by maximum likelihood (ML) principle. Then, the combined spectrum is rebinned with ML weights consistent with the expected distribution of the axion signal. Finally, the grand spectrum is examined for an axion signal by setting a threshold and rescanning the narrow bands where significant peaks are observed. It is essential to examine the combined spectrum to spot single- or few-bin-parasite lines caused by IF or RF interference as opposed to a wider distribution of a hypothetical axion signal or a statistical fluctuation. A real axion signal should have a specific linewidth and lineshape. The former is calculated to be around 10 kHz and the latter is expected to be a Maxwell–Boltzmann distribution. Observed linewidth will be further increased if the full width at half maximum (FWHM) value of the resonance mode is significantly bigger than 10 kHz. In addition to the two aforementioned properties (linewidth and shape), an axion signal will distinguish from interference lines by its consistent occurrence at a fixed frequency.

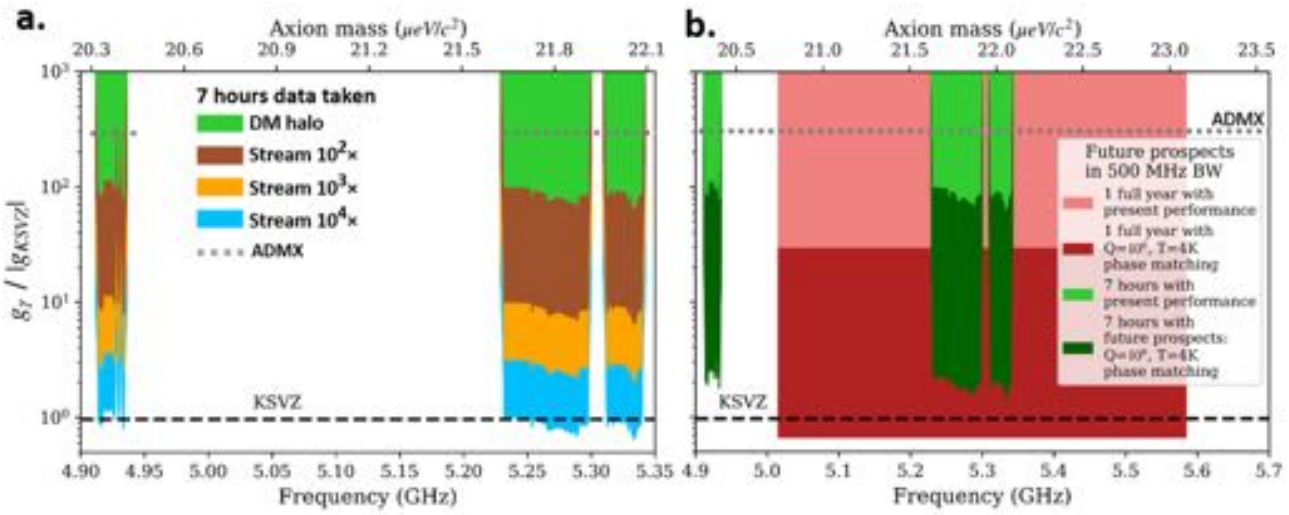

Figure 17: (**a.**) Exclusion plot tuning one CAPP cavity at a time assuming galactic halo DM axions and streaming DM axions. Measuring time ~7 hours. E.g., an axion signature could have been observed in case of an axion stream or axion cluster lasting for about 1 hour with a density ~10^4× the local DM mean value of 0.3 GeV/cm^3, and, for axions in this mass range with the theoretical coupling constant (KSVZ line). For comparison, it is given also the limit measured by ADMX [8]. (**b.**) Perspectives for future longtime measurements assuming the present and improved cavity performance, e.g., Q = 10^6 following recent development [6].

References:

[1] O.K. Baker, M. Betz, F. Caspers, J. Jaeckel, A. Lindner, A. Ringwald, Y. Semertzidis, P. Sikivie, K. Zioutas, *Prospects for searching axion-like particle dark matter with dipole, toroidal, and wiggler magnets*, Phys. Rev. D85 (**2012**) 035018; https://doi.org/10.1103/PhysRevD.85.035018
[2] K. Zioutas, V. Anastassopoulos, S. Bertolucci, G. Cantatore, S. A. Cetin, H. Fischer, W. Funk, A. Gardikiotis, D. H. H. Hoffmann, S. Hofmann, M. Karuza, M. Maroudas,Y. K. Semertzidis, I. Tkatchev, *Search for axions in streaming dark matter,* https://arxiv.org/abs/1703.01436 (**2017**).
[3] H. Fischer, Y. K. Semertzidis, K. Zioutas, Search for axions in streaming dark matter, EP Newsletter (**2017**); https://ep-news.web.cern.ch/content/search-axions-streaming-dark-matter.
[4] B.R. Patla, R.J. Nemiroff, D.H.H. Hoffmann, K. Zioutas*, Flux Enhancement of Slow-Moving Particles by Sun or Jupiter: can they be detected on Earth?* ApJ. 780 (**2014**) 158;
[5] H. Fischer, X.Liang, Y. Semertzidis, A. Zhitnitsky, K. Zioutas*, New mechanism producing axions in the AQN model and how the CAST can discover them*, Phys. Rev. D98 (**2018**) 043013 https://journals.aps.org/prd/abstract/10.1103/PhysRevD.98.043013 .
[6] D. Ahn, O. Kwon, S. Woo Youn, W. Jang, J. Lee, W. Chung, D. Youm, Y.K. Semertzidis, *Superconducting YBCO microwave cavity in a high magnetic field for axion dark matter search*, 15th PATRAS Workshop on Axions, WIMPs and WISPs, (**2019**); https://indico.desy.de/indico/event/22598/session/2/contribution/63/material/slides/0.pdf .
[7] D. Budker, V.V. Flambaum, X. Liang, A Zhitnitsky, *Axion Quark Nuggets and how a Global Network can discover them,* https://arxiv.org/abs/1909.09475 (**2019**).
[8] C. Boutan, et al., (The ADMX Collaboration), *Piezoelectrically Tuned Multimode Cavity Search for Axion Dark Matter*, Phys. Rev. Lett. 121 (**2018**) 261302; https://arxiv.org/abs/1901.00920 .

RADES relic axion detector

1. RADES prospects

The last prospect of the RADES data taking plans was given in January 2019. We are happy to emphasize that we succeeded in 2 major goals for 2019. Firstly, we managed to construct in time and install an almost 1m long alternating-irises cavity. Prospects on parameter reach are given below and all assume a signal to noise ratio of 3, respectively. Secondly, we are well on track on testing and implementing a tuning mechanism for the RADES-style cavities.

In 2019, we are taking data with a 30 sub-cavities alternating irises cavity of a length of approximately 1m. In the plot we assume Q=1200 (measured value), coupling beta=0.75 and (measured value), at a central mass of 8.37 GHz and thus a mass of m = 34.62 mu eV, a geometrical factor of G=0.55 (simulated value) as well as a data taking time of around 3 months (12 weeks). The measured Q value of the 30 sub-cavities alternating structure lies below expectation. Reasons for this are given in section 5.

Please note an important caveat: From Figure 1 is visible that the long alternating cavity is not much more sensitive than the short inductive. This is due to the low Q. However, on the long term, the volume is more important than the quality factor as the scanning speed for axions $\frac{df}{dt}\frac{f}{Q}$. This is why gaining volume in the prospect of tunable cavities is in principle more important than a large quality factor.

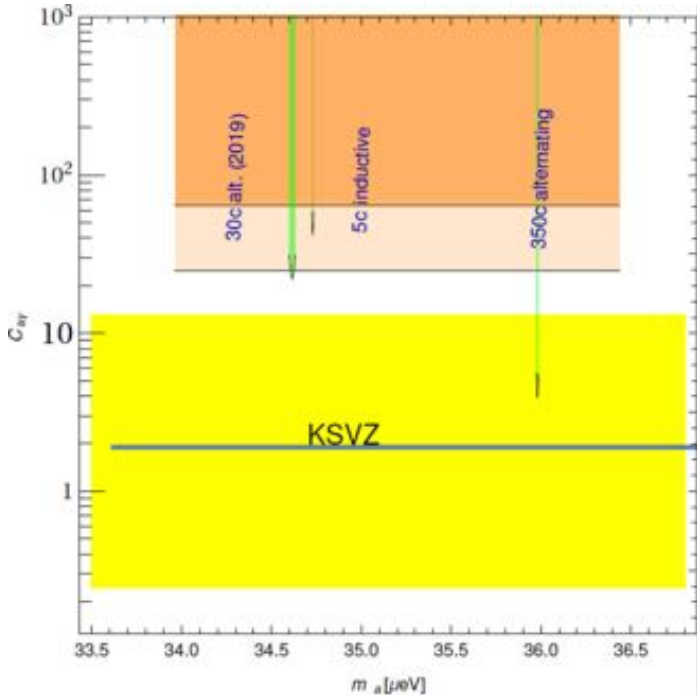

Figure 1 Prospects of reach in the axion coupling-mass plane with RADES type cavities. The yellow band denotes typical axion models and the KSVZ model is denoted with a blue line, the ``5-c inductive'' line is a prospect of existing 2018 data upon finalization of the analysis. The ``30c alt.'' line is a prospect of the reach with this year's data (2019). The orange areas denote prospects for a hypothetical short (2020) and long (2021?) tunable cavity, respectively. The ``350c alternating'' is a prospect for a hypothetical very long cavity built from individual modules (see text for details).

For 2020 we propose a short tunable cavity. The cavity with its tuning mechanism is currently being tested at CERN's cryolab to mitigate potential risks for 2020 data taking well ahead of time. The darker orange area in Figure 1 indicates this option. The outlook is similar to the January 2019 report: Assumptions is a tuning range of 600 MHz achievable in the cold. With a width of ~3 MHz we might

scan for 200 Steps in 24 weeks, i.e. ~ each 17 h for one scan step. We assume a conservative Q value of 6000 (but for this cavity type an even higher Q value up to 10000 could be reached)
For 2021 we have multiple possibilities. Firstly, we are considering modular cavities, as described in this report. We have observed that machining cavities beyond the 1m scale becomes unfeasible mechanically. Thus, we are conceiving modular cavities, i.e. small sets of sub-cavities that can be assembled flexibly for the bore length at hand. Secondly, we have the possibility of testing a longer tune-able cavity of max 1m. Given the importance of having a modular concept working for the future (e.g. for baby-IAXO), we will put emphasis of developing a modular type. Also, it has the better prospect of reaching realistic QCD axion parameters.
If the modular R&D is successful, we can aim for a up to 350 cavities version, as already detailed in the January 2019 report. With the modular concept we have now a realistic approach towards increasing the length. Also, phase-matching can be considered. If not, a 1m-tunable inductive irises prospect is presented as light orange area with realistic parameters.

1.1. Connection to babyIAXO

The SPSC requested to "coordinate the efforts also accounting the CERN contributions to baby-IAXO". Indeed, the RADES project has been conceived with the long-term goal of performing axion-dark-matter searches also with baby-IAXO.
The current babyIAXO design is such that an upgrade to a cold bore indeed is easily possible, as required for haloscopes but not the helioscope. The CERN babyIAXO magnet team consists of Herman Ten Kate, Alexey Dudarev and Nikolay Bykovskiy.
The crucial work in preparing babyIAXO for a future haloscope data-taking with RADES cavities will be to foresee interfaces and connectors to accommodate the RADES tuning feedthroughs and validate the tuning principle.
As the RADES tuning is being prototyped, regular meetings will be held between the RADES group and he CERN babyIAXO magnet team. The first meeting is scheduled for October 2nd. Also, a RADES presentation at the upcoming IAXO collaboration meeting will be the starting point for further regular technical discussions.
In conclusion, CAST is a unique opportunity to develop the needed experience in exploiting the full physics potential of babyIAXO.

1.2 Facing common critique

Let us use this section, to mitigate some concerns and critical questions raised in previous discussions of this proposal and point out some benefits, in addition to the above discussed physics case, for allowing RADES to continue to take data

RADES/babyIAXO transition
The current schedule of babyIAXO foresees data taking ~2023 with vacuum and gas phases. At a later stage, data-taking with RADES-type cavities would be foreseen. From this, it seems that RADES doesn't transition directly into activities within babyIAXO. However, two major points should be observed. Firstly, data taking schedule with RADES in babyIAXO depends on the readiness of the overall babyIAXO project. Thus, in principle, RADES data taking could be before a solar run, even if this is now not foreseen in the official time-line (e.g. if solar tracking becomes available only later). Secondly, the experience with CAST: live cryogenic, vibrating/sun-tracking environment with a strong magnetic field is unique and the development of expertise at CAST is probably mandatory to transition smoothly from solar data taking with babyIAXO to cavities. To have babyIAXO functioning as a haloscope, R&D at CAST is very timely

International competition
For this we refer to the June 2019 answers to the SPSC questions: To our knowledge there is no direct immediate competition at ``our'' envisioned mass-range if we manage to keep to our schedule

Usefulness of results in which we don't reach the QCD axion line
One common critique for RADES, is that, when tuning, it has difficulties in reaching the QCD axion line. This is true, only a prolonged data taking at a given mass allows to probe the QCD axion if we don't improve significantly in Q or the noise temperature. Two comments on this: Firstly, RADES searches in the high-mass axion region, in which predictions for the QCD axion mass from first principle are becoming more frequent (see e.g. *Nature* **volume 539**, pages 69–71 (03 November 2016)). As we learn to design our micro-wave filters we can become more confident in designing a cavity for an axion sweet-spot with an ultra-long modular RADES cavity. Secondly, for Axion-like particles there are few well-motivated predictions in the mass-coupling space but only astrophysical hints and theory motivation from UV-complete models. Nevertheless, one of the axionic flag-ship experiments ALPS-II is being built with a great effort to improve sensitivity by 2 orders of magnitude in coupling but no chance to discover the QCD axion. RADES scans a much smaller mass range than ALPS-II but at much weaker couplings and lower cost and is thus one of the few experiments that can aid in exploring the parameter space for ALPs, at small coupling and high-mass.

``Interdisciplinary'' research. Usefulness of RADES results beyond axions
Tuning with ferro-electrics and the properties of copper at 2K are of interest, e.g. for industry (we are regularly in touch with EUCLID Techlabs on these issues. Also, we are in touch with a group at Aalto university to work together on single microwave photon detection

Funding
Besides a part of ERC 802836 that among else enabled to hire one of the currently 4 PhD students within RADES, we are currently drafting funding proposals within Spain on the order of 100k Euro. This will allow, e.g. to develop a better DAQ system for RADES and build future cavities.

2. Vertical cut cavity: mechanical tuning mechanism

Three different designs for a mechanical tuning were discussed. The first two ideas included a piezo actuator to move the two cavity parts. The third idea is to move one part of the cavity via gears from the outside at ambient conditions. The advantage of the third version is that a motor can be mounted outside of the magnet at ambient temperatures. This makes it possible to access the motor during the data taking period and exchange it in case of problems. Furthermore, a motor which does not require to work at UHV and low temperatures is less expensive. This is why the version with the gears will be realized and a prototype will be tested in the CERN Central Cryogenic Laboratory.
The gears and gear rack for the prototype are made out of acetal. A mock-up for the tuning was built to test the gears and the gear rack separately. With the mock-up, it was demonstrated that the gears can move a 100 g metal piece at cryogenic temperatures and that the material acetal resists a few cool-downs to 77 K and still works afterwards.
A 3D exploded view of the mechanical tuning mechanism is shown in Figure 1 (left). The parts of this design were produced at the CERN main workshop and are shown in Figure 1 (right). The elements are made of stainless steel and aluminium because of the low friction coefficient of 0.3 between these two materials (friction coefficient in vacuum: Stainless Steel-Al = 0.3; Al-Al = 1.6-2.2; SS-SS = 2.9). First tests of the mechanism at room temperature and cryogenic temperatures are planned for September/October 2019 in the CERN Central Laboratory.

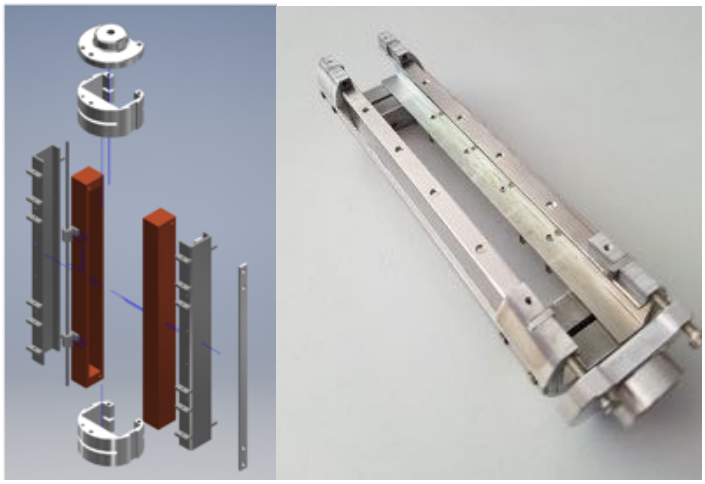

Figure 2: 3D exploded view of the mechanical tuning mechanism (left) and prototype of the tuning mechanism (l= 16.5 cm, radius = 4.0 cm) made of aluminum and stainless steel (right).

3. Ferroelectric tuning mechanism

The studies for the ferroelectric tuning mechanism have also advanced. After consulting with ferroelectric experts, it was determined that STO material would work and the conditions presented in the CAST magnet (the quantum paraelectricity effect is now discarded). However, its permittivity is extremely high, so we need to find the best position in the structure to avoid a poor C (trade-off between form factor and tuning range). For this reason, we decided to simulate the behaviour of the RADES six cavity structure loaded with a ferroelectric of extremely high permittivity at the middle capacitive iris. With such an idea, we obtained a 45 MHz tuning range with a form factor degradation below 15%. In Figure 3 we can see a frequency shift obtained with a change of the permittivity between 3000 and 7000.

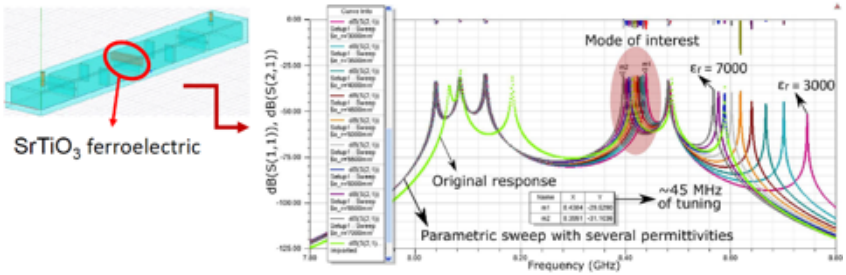

Figure 3: Simulation of SrTiO3 used as capacitive iris. The transmission parameter was simulated for different permittivity.

Another interesting idea with ferroelectric is being studied: tuning with temperature, employing heating cables attached on the outside of the detector increasing/decreasing a pair of degrees the entire structure. The ferroelectric permittivity is also affected by the operation temperature. With such an idea, we introduce a little noise temperature T_{sys}, but we avoid the introduction of extra feed cables inside the structure.

4. Vertical cut cavity: Coupling, Q_0 and el. conductivity at cryogenic temperatures

With the cryogenic set-up described in the last SPSC-report it was possible to monitor the Q-value and the coupling change between 7 K and 300 K. Three measurement runs have been performed in the CERN Central Cryogenic lab. For the first measurement run one port was chosen to be near critically coupled at ambient temperature (β = 1.6). The final goal of these measurements is to do determine the antenna length needed to get a critical coupling at 7K, which is necessary for an optimal axion detection. The S-parameters were measured during the cool down of the system.

Figure 4 (left) shows the increase of the coupling factor β during the cool down. For this measurement, the gap of the vertical cut cavity was closed. The coupling increases by a factor of about 4.4 to a beta

of approximately 7.0. Using this measurement to predict the critical coupling (meaning β = 1) for the cavity at cryogenic temperatures from the coupling measurement at ambient temperature the coupling at room temperature should be around 0.23. For the second measurement run at cryogenic temperatures the coupling at port 1 was 0.337, thus at cryogenic temperatures a coupling of about 1.5 is predicted. In Figure 4 (right) the coupling for this measurement run is illustrated, the gap of the cavity was also closed in this measurement run (closed (2)). The coupling changed from 0.337 to a beta of about 1.7, which is close to the predicted value.

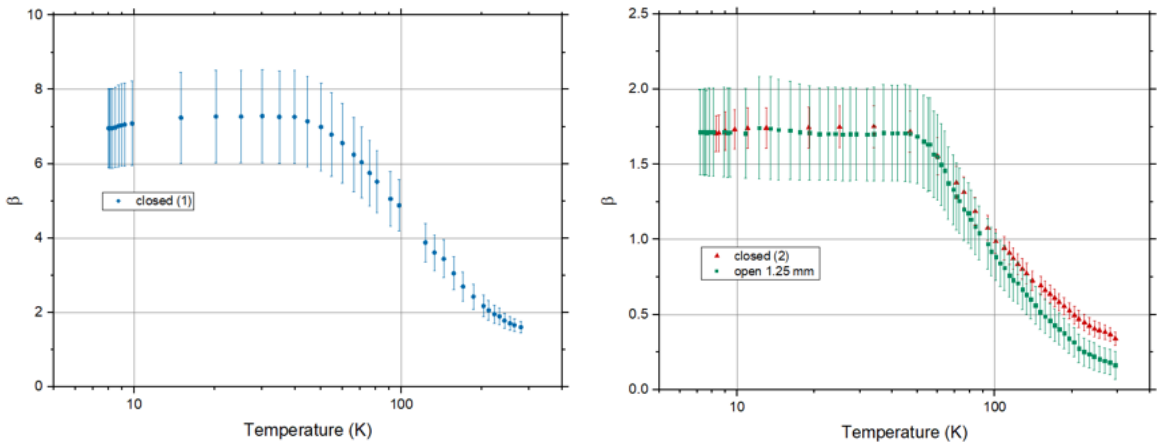

Figure 4: Coupling factor β vs temperature between 7 K and 300 K. Left: Measurement helping to predict the antenna length for critical coupling at cryogenic temperatures. No gap and β=1.6 at room temperature. Right: Shows that we achieved almost critical coupling at cryogenic temperatures for the no gap measurement and that the coupling is the same with a gap (no gap = red triangle; 1.25 mm gap = green rectangle).

In addition to the two measurements investigating the coupling factor a third measurement was performed opening the gap of the vertical cut cavity. For this measurement run the antenna at port 1 was not changed. The gap size was chosen to be 1.25 mm. The corresponding coupling factor for the open cavity is also shown in Figure 4 (right (open 1.25 mm)). Since the antenna length was not changed a similar coupling was expected for this measurement. Within the error bars the coupling at cryogenic temperatures is the same for closed (2) and open 1.25 mm measurements.

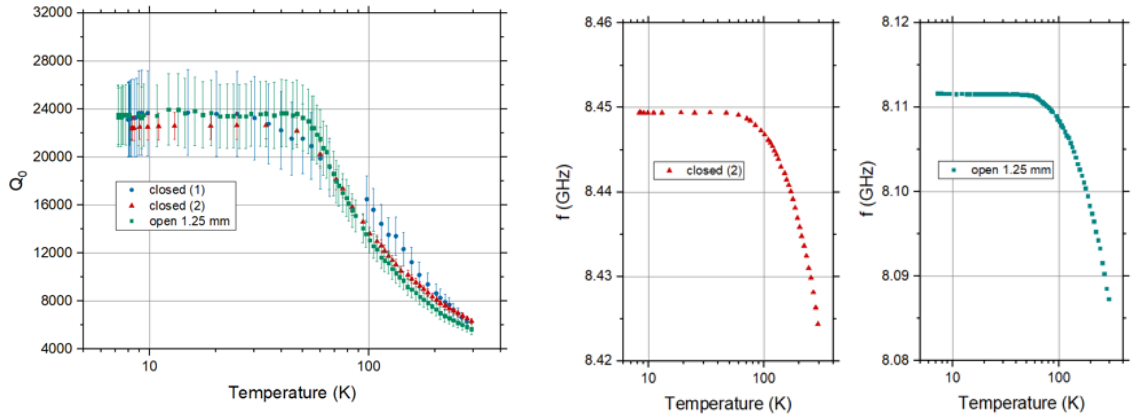

Figure 5: Q_0 and frequency vs temperature between 7 K and 300 K for different coupling and gap opening (closed and 1.25 mm opening).

Figure 5 (left) shows the Q_0 values versus temperature for all three measurement runs. The quality factor increases with decreasing temperature and saturates at about 40 K. The quality factor at cryogenic temperatures is about 24 000 which corresponds to a conductivity of copper of about 10^9 S/m. The value for the conductivity will be used for future simulations. Because of the anomalous

skin effect the electrical conductivity of copper does not increase further below 40. All three measurement configurations give the same Q_0 values within their error bars. That even the measurement with a 1.25 mm wide gap has the same quality factor proofs that a mechanical tuning by increasing the gap of the cavity should work.
The frequency change versus temperature is illustrated in Figure 5 for the measurement with the cavity closed (middle) and 1.25 mm open (right). During cool down the resonance frequency changes by approximately 25 MHz. The resonance frequency of the 1.25 mm open cavity is 338 MHz lower than for the cavity in closed position (f = 8.449 GHz) at cryogenic temperatures.

5. Small setup upgrade at CAST

Apart from our new 30 cavity structure (see next section) some upgrades were performed on the RADES setup. In order to bypass the low noise amplifier (LNA) and measure the antenna coupling at our signal port, an RF switch was installed. This switch was installed and tested successfully in April, allowing the first in situ measurement of the coupling. Furthermore, new flexible SMA cables were acquired and used to make the connection inside the copper vessel. With the addition of the new switch the space inside the vessel was very limited, these new cables have a smaller diameter and enough flexibility to adapt to these conditions. The semi-rigid cables were more easily damaged during the bending needed for the installation, increasing the chance of a malfunctioning of the transmission line. In addition, the new cables allowed a faster and easier installation (see Figure 6). The broken temperature sensor cable was fixed during this year installation and now the temperature of the cavity has been recorded during the cool down process. Reaching for now a temperature of 3.9 K before the last quench test. All of these features give a better control of the system and allow a better quality control of the data that will be taken in 2019.

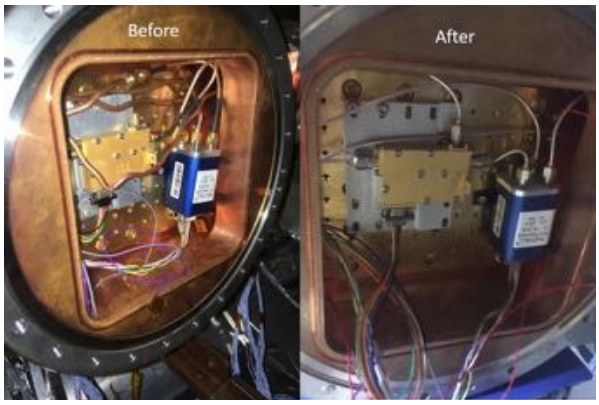

Figure 6: RADES copper vessel, left: test installation in April right: Final installation in July.

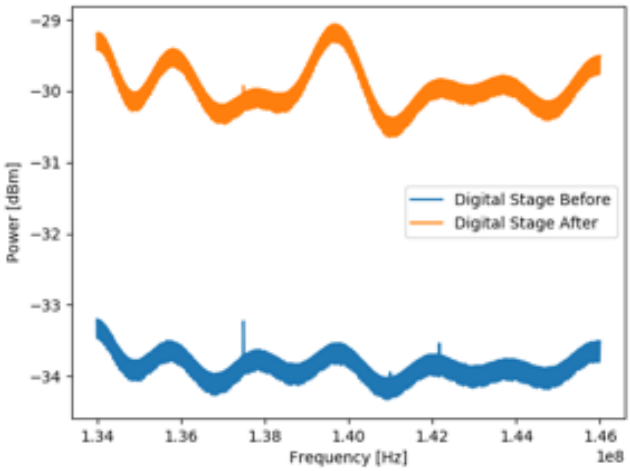

Figure 7: Spectrum of the digital stage. The blue line (90s of integration time) was before the introduction of the adapter plate. The orange (93s of integration time) is afterwards.

Finally, the performance of our digital stage has improved. The problem with the noisy bins produced by it has been mentioned already several times in the past SPSC. The stage was sent back to vendor (TTI in Spain) in the beginning of June. After several tests, the company found out that the intrinsic spurious signals from the AD convertor were enhanced by the transmission line used for the Ethernet communication between the FPGA and the computer. This problem was solved by introducing a HW adapter plate between the FPGA and the AD convertor. Most of the spurious bins were eliminated (see Figure 7) except for one at 137.5 MHz. The reason for this spurious signal was not found by the company, but they were asked to send back the digital stage because of the start of the data taking at CAST.

6. New alternating 30-cavities structure

One of the biggest challenges of the RADES group is to increase in volume to take advantage of the long bore of the CAST magnet. For this reason, the main goal for 2019 was to install a longer cavity. Designs and simulations were done at the end of 2018 and beginning of 2019 to start with the production and have it ready for the installation period. From the start it was pointed out by both of the workshops that we contacted that producing such a cavity is difficult and the tolerances we had used until now (30 microns) cannot be used for the longer cavity (at the end 100 microns of tolerances had to be used). The cavity was ready just in time to install it inside of the CAST magnet. Figure 9 compares the size of the previous cavity with the one installed this year. The production was done by the CERN main workshop.

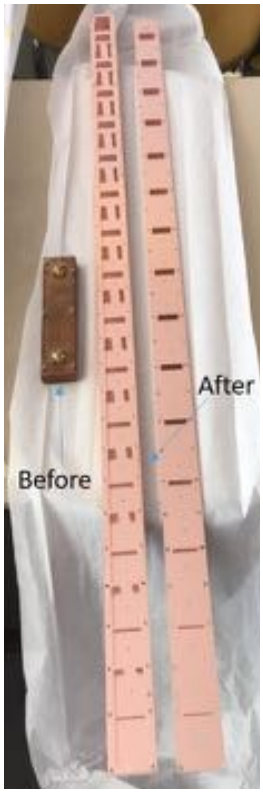

Figure 8: Comparison of the 2018 cavity prototype (left) with the new 30 cavities structure (right)

During the cool down of CAST the scattering parameters of the 30-cavities structure were measured and the coupling and Q-values calculated. The scattering parameter S21 in dB is illustrated for different temperatures in Figure 9. The mode to which the axion couples is marked with a black arrow.

For the marked peak the frequency change, the coupling β and the quality factor Q_0 during the cool down for the alternating cavity was calculated. The frequency changed 28 MHz by cooling the cavity down from 300 to 5 K. This was expected due to the geometry change of the cavity.

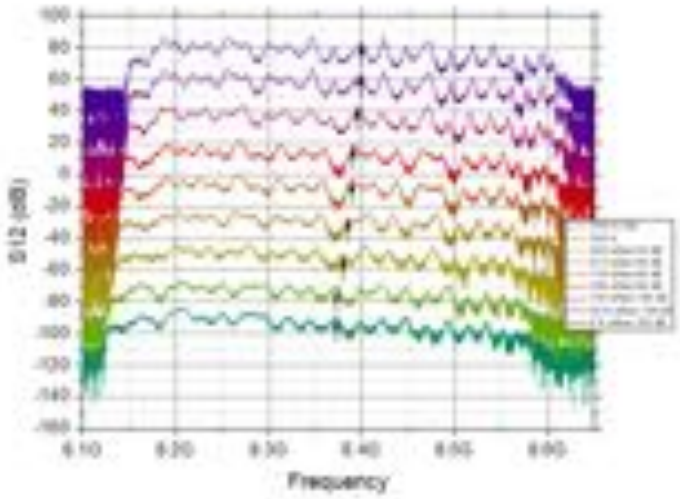

Figure 9: S21 measured during the CAST cool down at different temperatures for the alternating 30 cavities structure.

In Figure 10 (middle), the change of the coupling with temperature is illustrated. From the cryogenic measurements of the vertical cut cavity, we had learned how much the coupling change during cool down. This is why we chose an under coupling of about β=0.1 at ambient temperature, aiming for a β=1.0 at 4 K for the alternating cavity. The coupling measured at 5 K is about 0.75 (under coupled) which was a great success even so we did not reach fully 1.0, but we are very close considering that the alternating structure had some additional losses compared the vertical cut cavity, which made the estimation of β at cold more difficult. The change of the quality factor Q_0 is shown in Figure 10 (right). The quality factor reached at ambient temperatures only 1200 and increased to about 2000 at cold. Due to additional losses which might come from a gap between the lid and the cavity, the predicted value at room temperature of $Q_0 = 6000$ was not reached. Since these losses do not decrease with temperature a Q_0 of about 2000 at 5 K was expected.

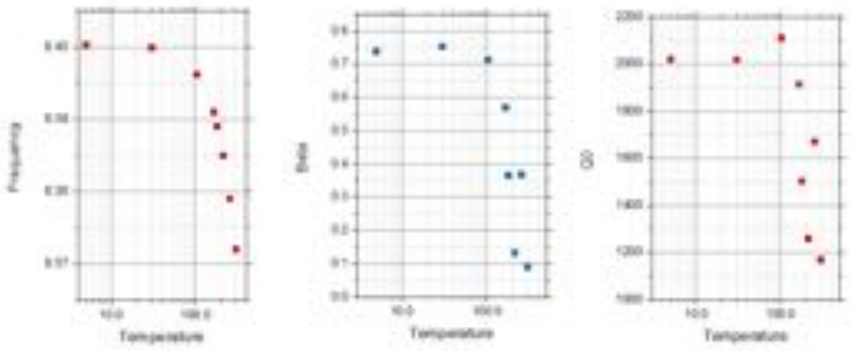

Figure 10: Frequency, coupling and quality factor measured during the CAST cool down at different temperatures for the alternating 30 cavities structure.

At the moment, we are investigating the reason for this unexpected low Q-value. The small version (with six cavities) of the alternating structure also presented a lower than the expected Q - value. Tests were done to this cavity pointed out that the contact between the cavity and the lid is not ideal. This is having a bigger influence on the capacitive irises in comparison with the inductive irises. This is the reason why the 5-cavities structure does not suffer that much from this contact problem. The long structure is installed at CAST, but the smaller version is sitting in the lab and tests and simulations are undergoing to see how to solve this issue. The main workshop is introducing approximately 30 more screw holes in order to improve the contact. A gap has been introduced in the simulation in order to see the effect of it in the scattering parameters (see Figure 11).

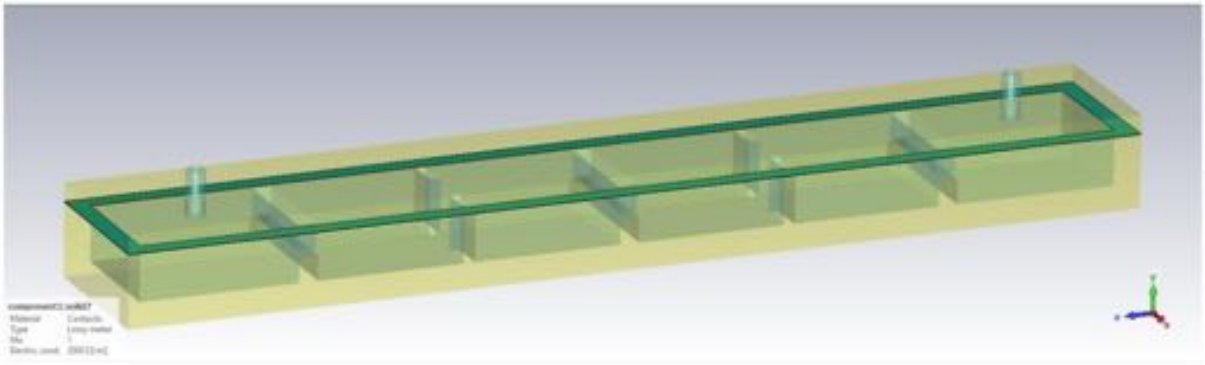

Figure 11: Introduction of a gap in the CST simulations to see the effects of a bad contact between the cavity and the lid.

This issue and the fact that the workshop will have to work with even bigger tolerances in case of a two or 3 meter long cavity showed that it is better to make a small adjustment to the approach when constructing this cavity. For this reason, it was decided to focus part of work for the development of modular structures than then can be connected together.

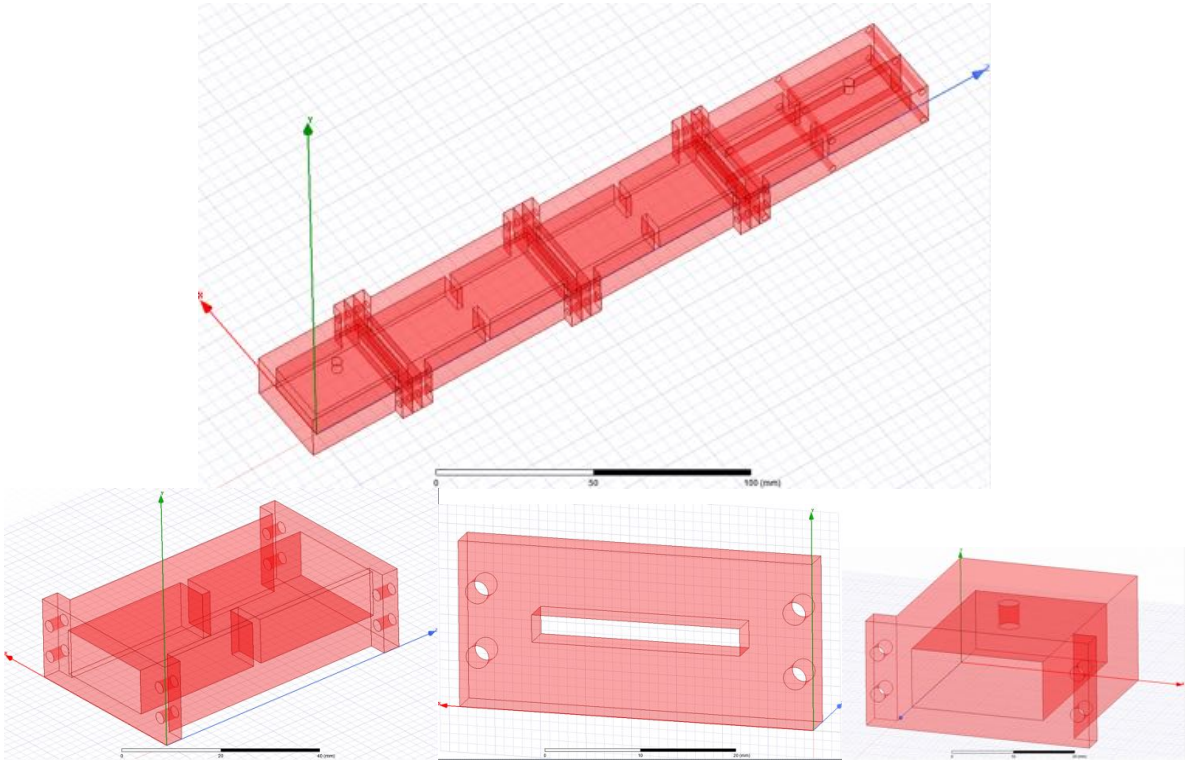

Figure 12: Modular cavity 3D model. Top: Seven cavities model assembly. Bottom left: inductive cavity module. Bottom middle: Capacitive iris. Bottom right: First and last cavity module.

Figure 12 shows the first conceptual design of modular structure. The cavity will be build using individual modules. This brings many advantages with it; the first one is that the modules can be done with 30 microns of tolerances. The machines to produce these small pieces are easily found in most of the workshops in contrast to the special machine need to produce the 30-cavity structure. This will reduce the time of production. We will not need to start from zero every time we want to increase the volume, we will just add more and more modules to the current cavity. The inductive iris modules will be produced using a vertical cut, which already showed very good Q-value results (see section 1), while the capacitive irises are produced separately without a lid. This should also improve the actual Q-value for an alternating structure. We will focus on the production and characterization of this idea during the end of 2019 and most of 2020. If the R&D works fine then, with this idea we will try to aim for the production of a 350 cavities structure in 2021.

7. Data analysis update

The data analysis procedure has been slightly modified to follow the latest analysis procedure presented by the HAYSTAC group (https://arxiv.org/abs/1706.08388), which is a standard in the axion haloscope community. Figure 13 shows a summary of the main four steps of the analysis. First, the average spectrum is built and the Savitzky Golay (SG) filter is applied to it (Figure 13: top left). Afterwards, each spectrum is divided by this filter. The noisy bins are then removed and a second SG filter is applied (Figure 13: top right). Then, each spectrum is divided by its corresponding SG filter to produce a unit-less normalized spectrum (Figure 13: bottom left). Finally, all spectra are combined to produce a grand unified spectrum (GUS) (Figure 13: bottom right). Later on, the GUS spectrum and its standard deviation are used to search for a possible axion signal above a given threshold (see Figure 14). If no bin is above the threshold, the standard deviation can be used to produce the exclusion limit (see Figure 15). However, the exclusion limit here is not final. The results given by this plot exceed the expected theoretical value for 14 hours of data taking (the amount used for this analysis). The code and the analysis are under study now.

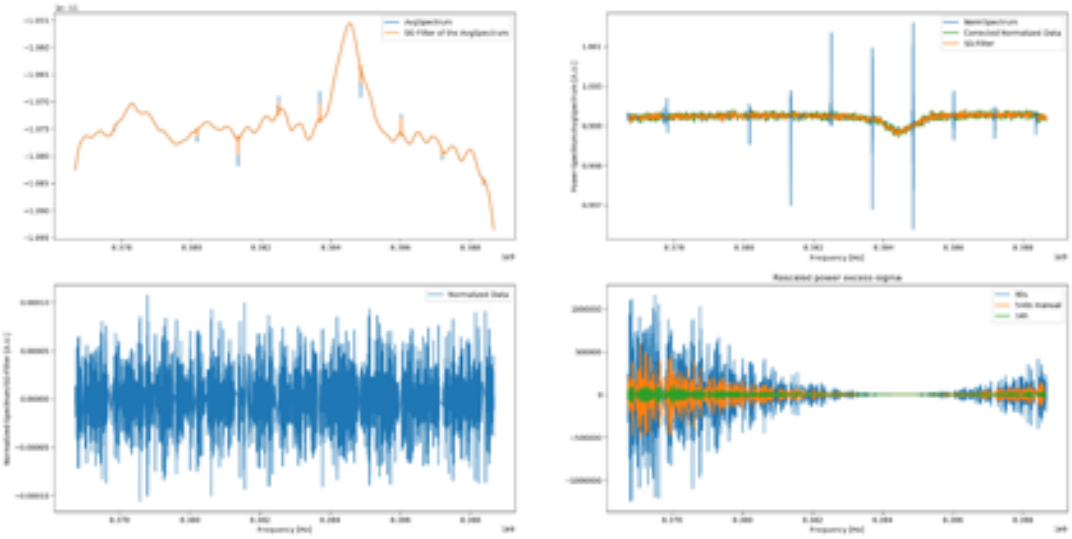

Figure 13: Top-left: 14h average spectrum (blue) and the SG-filter of it (orange). Top-right: One spectrum divided by the SG-filter of the average (blue), after the removal of the noisy bins (green), the SG-Filter of the corrected normalized trace (orange). Bottom-Left: Division of the corrected normalized trace by the SG-filter and subtracting 1. Bottom-right: Re-scaled GUS obtained by multiplying it by the noise power and the inverse expected axion power, a 90 second trace (blue), a 540 seconds measurement (orange), the 14 hours set (green).

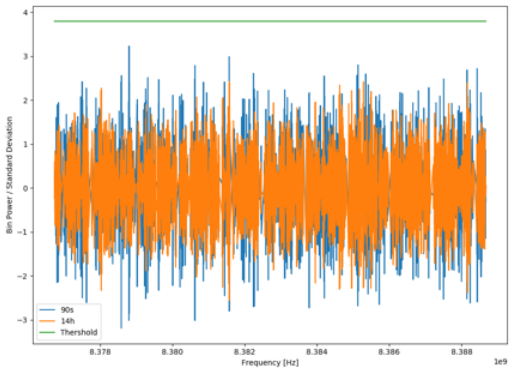

Figure 14: Measured power at each bin divided by the standard deviation. Blue line for 90 seconds and orange line for 14 hours. The green line marks the threshold for any possible axion signal.

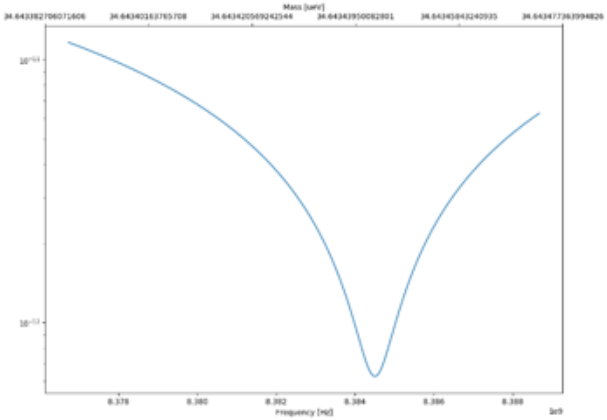

Figure 15: Preliminary exclusion limit of 14 hours of data.

Solar Axion Search

A new solar axion data taking campaign at the CAST sunrise end with the IAXO pathfinder system

Summary

We propose to resume solar axion searches at the sunrise end of CAST with the IAXO pathfinder system, composed by the new LLNL X-ray telescope (XRT), with improved low-background and low-threshold gas detectors (both the microbulk and the GridPix Micromegas detectors). The goal of the proposal is to:

1) improve the result obtained in the 2013-15 phase on $g_{a\gamma}$
2) clarify the statistical/systematic origin of the 2σ-excess observed in the sunrise Micromegas (SRMM) data set;
3) get insight into the limitations of current detection parameters (background and threshold) in both microbulk and GridPix technologies; and
4) provide technical and operational experience for the future babyIAXO and IAXO

Preliminary Considerations

The last vacuum solar axion data-taking campaign of 2013-15 has been a success, providing the best limit so far on $g_{a\gamma}$ by CAST. The resulting paper in *Nature Physics* will remain as a legacy publication of the CAST experiment. The improvement with respect to the previous CAST vacuum result has been allowed by the recent achievements on low-background of the Micromegas detectors, plus the construction of a new, axion-optimized, XRT for the SRMM system. In particular, the XRT+SRMM performance has met all expectations. It has proven the combination of both focusing and low-background concepts, previously tested in CAST only separately. This has led to the best signal-to-noise ratio (SNR) of any previous detection system of CAST. The effective background level (number of background counts expected in the energy- and focal-area-region of interest) is of about 1 count per 6 months of operation of the experiment (~0.003 counts/hour).

However, the relatively low statistics collected with this system in the 2013-15 campaign (290 tracking hours) makes the result statistics-limited, which partially hinders its impact in the overall limit. In addition, the data revealed 3(4) detected counts in the 95% (99%) signal-enclosing region, while only ~1(~2) was expected. Although this observation can still be a statistical fluctuation of the background (at ~2σ), the possibility of a non-statistical origin of this excess would be very important to dilucidate in view of the low-background limits of this technology. Such a possibility could be tested by additional statistics at CAST.

The current understanding of the background limitations of microbulk detectors allow to devise a number of steps to carry out in the quest for even lower background levels. In addition, the past experience with the GridPix detector has demonstrated capability for very low threshold, while the 2017-20118 activity has helped in applying the low background insight in this technology too. A roadmap of improvements for the GridPix detector is also foreseen. The opportunity of operating these systems at CAST would offer a realistic environment to validate such improvements.

In view of the above, it seems desirable to increase data-taking with the SRMM+XRT system. In this section we discuss the motivation, physics and technology-wise, of such a plan, as well as a concrete proposal in this direction.

The solar axion case after the last CAST results

1. The current CAST limit on $g_{a\gamma}$ has reached a value that competes with the best astrophysical bounds (coming from HB stars). This means that CAST is now sensitive to realistic ALP models not excluded by other arguments.
2. Moreover, current CAST sensitivity is bordering the region where models are invoked to solve a number of observational anomalies. The same HB stars limit mentioned above are the upper

bound of a result (hint) that mildly favors a hint of non-zero value of $g_{a\gamma}$. Similar hints come also from faster-than-expected cooling rate observed in white dwarfs, RGB and neutron stars.
3. At the low mass part of the parameter space, the current CAST bound borders on the region of values invoked in the issue of the transparency of the Universe to high-energy γ-rays.
4. In view of the above, further improving CAST sensitivity, even if in a modest extent, is a worthwhile effort.

The proposal

1. We propose to re-commission the SRMM+XRT system in CAST and plan a new data-taking campaign targeting about ~20 months of effective exposure, that could presumably be accommodated in 3 annual campaigns, given that *this activity does not conflict with CAPP and RADES runs*. The total exposure time should be shared between the microbulk and the GridPix detectors. We aim to at least 13 months of data taking with similar or better detection parameters to the ones enjoyed by the microbulk detector in 2015, in order to multiply ×3 the existing SRMM statistics. A time slot of 1-2 months could be reserved to test other detector technologies, interesting for babyIAXO. The exact periods for GridPixmicrobulk will be determined later on by the proponent groups in accordance with the progress and improvement plans on the detectors.
2. The XRT, Microbulk detector and shielding are already reinstalled in CAST and are ready for data-taking and therefore this proposal does not rely on any important investment. The proponent groups need to find resources for maintenance and operation of the systems in CAST during the proposed period, shifts, etc. which seems feasible.
3. A number of technical improvements on the detectors side are under consideration that are being carried out as part of the preparatory phase of future experiments. They could come on time for the campaign in CAST, on a best effort basis. They include:

For the microbulk detectors:

a) Change the detector gas to a Xenon mixture, instead of Argon. This may improve the background of the detector (see Figure 2 and its caption). In addition, Xe allows for higher detection efficiency than Ar, and therefore it can be used at lower pressure. A pressure of ~500 mbar of Xe could offer similar efficiency to X-rays that our current 1.4 bar of Ar. This brings two additional practical advantages: i) gas amplification is higher at lower pressures, leading to lower detection energy threshold, and ii) a lower gas pressure puts less mechanical constraint to the window, maybe allowing to go to thinner versions (increasing efficiency to lower energies)

b) Change to a self-triggered DAQ electronics based on the AGET chip. It will improve the hardware threshold of the detector, currently limited by the high-capacitance (and thus relatively noisy) mesh signal.

c) Following experience from the GridPix detector, and taking advantage of the small photon entrance by the XRT, go to thinner and smaller x-ray windows to decrease detection threshold and increase efficiency at low energies.

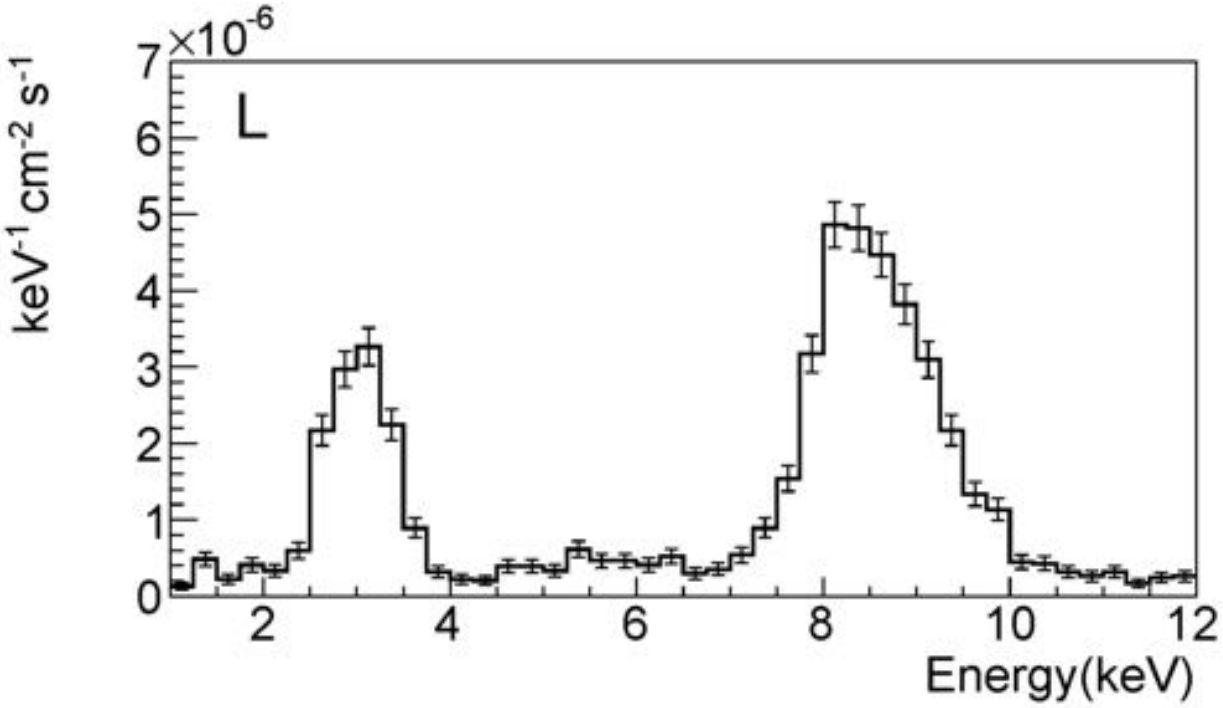

Figure 2: Background spectrum of the SRMM detector during 2015. The peak at ~3keV corresponds to Ar fluorescence and the ~8keV to Cu fluorescence. More than half of the background counts in the 2–7keV region are in the3keV peak. Replacing Ar by Xe in the detector would make this peak disappear and presumably further reduce background. In addition, the contribution from the β-decay of the naturally occurring ^{39}Ar isotope, estimated to about 10^{-7} counts/keV/s/cm^2, would be avoided.

For the GridPix detectors:

a) Go to larger detector areas (comparable to microbulk detectors), and exploit background reduction obtained by filtering multisite events.

b) Improve low-background capabilities of the detector, both by shielding and radiopurity of components.

Goals

The goals of our proposal can be stated in the following four points:

1. The additional data taken, combined with our previous result, will improve the sensitivity of CAST to $g_{a\gamma}$. Although modest, as argued before, this improvement will further push our current limit into unexplored and interesting values of $g_{a\gamma}$. We consider it worthwhile of the effort and likely to lead to a publishable result. Figure 3 shows the average upper limit expected versus exposure time assuming identical detection parameters (background and efficiencies) as the one of the SRMM+XRT of the 2013-15 campaign.
2. Although the excess observed in the 2013-15 data (see above) is still compatible with a statistical fluctuation of the background, it nevertheless shows a 2σ tension with background only expectations. In the event that these counts were of non-statistical origin, its determination would be of utmost importance (in the case of an axion-like signal, for obvious reasons, otherwise because its understanding would be crucial for additional improvements in background). Such a case could be revealed in the data-taking proposed, or alternatively, the fluctuation could be statistically washed out.
3. The recent experience with GridPix detectors demonstrates that very low energy signals (well below keV) are detectable in gas, thanks to the extremely low capacitance of the GridPix pixelated readout (in this respect, current microbulk detectors have been limited by the baseline noise of the high-capacitance mesh electrode used to trigger the detection). In addition, the recent calibration data of the XRT shows good reflectivity figures (and therefore

good focusing capability) down to sub-keV energies. This puts the spotlight on the X-ray windows (both the detector and the differential vacuum window), as the main element driving the detection threshold in these systems. This year GridPix will operate without differential window, and with especially developed thin window in the detector. We propose to pursue the quest for lower energy threshold in the new campaign, both with GridPix and microbulks (see technical improvements above). This could open the window to new steps in sensitivity to other WISP- channels at the low-energy end of the spectrum, like electron-mediated axion production, chameleons, or other –still poorly studied– signals like ALP dark radiation. In addition, the development of low threshold detectors in helioscopes is motivated by the capability of deter- mining the axion mass in some cases of positive detection.

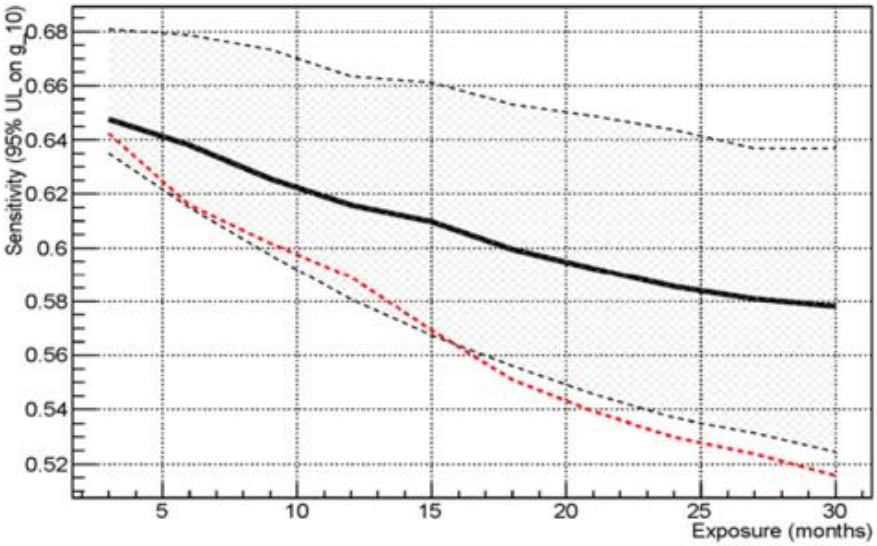

Figure 3: Projected sensitivity of XRT+SRMM system versus the additional exposure considered. The solid black line represents the average upper limit of 1000 statistical outcomes under the only-background hypothesis. The dashed area encompasses the 5% and 95% quartiles of the distribution of upper limits obtained, illustrating the statistical spread expected around the average. The red line represents the upper limit for the case of zero counts detected. The analysis assumes all detection parameters (efficiencies, background level and shape) as the 2015 SRMM system, and takes into account previous CAST results, i.e. it directly shows the improvement expected after a given additional exposure.

More generally, the proponent teams are active in developing and implementing new improvements for the detectors, in terms of lower background, threshold and higher efficiency. Some of these have been described above. The operation of both microbulk and GridPix detectors in CAST will be extremely helpful for the consolidation of such improvements, and the exploration for new ones. CAST provides the closest conditions to the ones of babyIAXO, being thus the ideal platform to test those improvements, while the extensive and thorough data processing, necessary to achieve the very low background levels, will also include physics outcome.
More in general, the operation of all the systems is of direct interest for the future IAXO experiment and would allow to produce relevant feedback for the preparatory phase.

Towards Implementation

1. The XRT and Microbulk detectors have been already installed and commissioned in CAST, anticipating the technical requirements associated with this proposal, while data taking has started in September 2019.
2. The responsible teams are currently active in continuously developing improved versions. The actual Microbulk detector is installed with the AGET front-end electronics (FEE) and the existing gas system with Argon based gas mixture. The upgrade to the Xenon gas system will start after the demonstration of the performance of the new FEE.

3. The proponent groups need to secure the resources needed to maintain the systems in CAST (installation, calibration, etc.) as well as to participate in shifts. This seems feasible if the proposal is positively considered. The proposed activities in Table 1 imply expenses that are covered internally by every group. The proponent groups have the right expertise to cover all needed aspects of the proposal as stated in Table 1.
4. Negotiations with the new groups from IRFU/CEA, DTU, LLNL and Columbia are under way to affiliate with the CAST Collaboration.

Table 1: Contribution of each institute to the program.

Institution	Contributions	Physicists
IRFU/CEA	Contribution to the new Micromegas gas system. Installation of the Sunrise Micromegas detector. Responsiblity for detector emergencies. Participation in the data taking. Participation in the data analysis.	I. Giomataris T. Papaevangelou E. Ferrer-Ribas
DTU, LLNL, U Columbia	Contribution to the alignment of the telescope. Ray-tracing codes for the focusing spot position and extension, significance of measured data at a given location in the detectors for current alignment. Participation in the data taking. Participation in the data analysis.	M. J. Pivovaroff J. K. Vogel J. Ruz Armendariz
RBI	Data taking coordination. Participation in the data taking. Participation in the data analysis.	B. Lakic K. Jakovcic
U Bonn	Improved InGrid system. Thin X-ray windows for MM and InGrid. Participation in data taking and analysis.	K. Desch J. Kaminski
U Zaragoza	Operation of the Micromegas detector (calibrations, quick look, data flow). Participation in the data taking. Data analysis.	I. G. Irastorza T. Dafni G. Luzon J. M. Carmona

Dark energy searches

In addition to Dark Matter and Axion Physics, CAST has also entered the quest to identify a possible Dark Energy candidate, chameleon fields being the most favored ones. We look for a stream of chameleons, produced in the sun by the Sikivie effect, reaching the Earth. These particles have been searched for by CAST through their photon-interaction channel with the GridPix detector, and could be detected with the KWISP force sensor exploiting their direct interaction with matter.

GridPix detector

1.) Detector:

The new detector had been installed in November 2017 and was smoothly taking data until March 2018. This period is called 'Run 2' in which 68 solar trackings (106 h), 107 h of calibration data with an ^{55}Fe source and 2401 h of background data were recorded. After some maintenance work done at Bonn, the detector was remounted on CAST in October 2018 and operated until December 2018, which we call 'Run 3'. In this period 47 solar trackings (74 h), 87 h of calibration data and 1125 h of background data were recorded.

While the GridPix readout worked smoothly, some of the new, auxiliary components of the setup did not yet work as expected during Run 2, but could be fixed and were fully available in Run 3. In the following, the detailed status of the detector components and their performance is described:

a) 7 chips readout: The GridPixes worked smoothly and hardly any discharges were observed during Run 2 and 3. During Run 2 several minor problems appeared, which did not influence data taking: the temperature readout stopped working, because a connector was ripped off, and the internal test pulse calibration malfunctioned, which was fixed and performed after Run 2. These minor problems were fixed in April shutdown and everything worked well in Run 3.

It was observed that the collected charge and number of pixels for a fixed energy (for instance the peak of the calibration data) fluctuates stronger than expected in time. The time constant of these fluctuations is rather large (of the order of hours to days). Partly this was related to a bad soldering joint on the ground line of the detector. This was fixed in April 2018. However, similar behavior (although not as strong) appeared in the CDL data taking in February 2019, despite all measured parameters being stable (temperature, gas flow, high voltage). The full reason for this and the impact on the analysis is still under study.

b) FADC readout: The FADC was implemented to record the time structure of the induced grid signal. This could help to identify cosmic ray particles passing perpendicular through the GridPix and leaving an X-ray like signal around 8 keV in the detector. It worked well except for some short periods where a high level of noise was observed. Since the readout is stopped, once the FADC triggers, this noise not only influences the grid signal itself, but also increases the deadtime of the detector. The standard readout cycle for the GridPixes consists of a 2.41 s frame with a readout time of 0.175 s resulting in a deadtime of approximately 7 % in absence of FADC triggers. At times of increased noise, the dead time increased considerably. However, since only short time intervals were affected during solar tracking, only a small amount of data was lost. During the investigation of the (intermittent) noise source, recabling and introducing HF-filters in the power supply lines did not help. It was found, however, that increasing the integration time of the preamplifier from 50 to 100 ns eliminates the impact of the noise completely. A first study shows that the impact on the physics performance is negligible and the shaping of 100 ns gives the same background suppression.

c) Field cage: The field cage was installed to improve the electric field homogeneity in particular in the drift volume above the outer 6 GridPixes. No problems were observed and the current through the resistor chain was as expected and stable.

d) Thin entrance window: The window breaking shortly before the data taking in 2017 (see previous report) had no significant impact apart from delaying the startup by a few weeks. No contamination of the telescope and no damage to the radioactive source were found. After replacement of the broken window, the detector could be reinstalled and data taking was started.

e) Piggy-back scintillator on the detector behind the GridPixes: This veto scintillator was installed to identify to cosmic ray particles passing through the GridPix detectors. Though tested extensively in Bonn, signals at very high rate were recorded during the 2017/18 data taking. The problem was identified and the scintillator performed as expected during Run 3.

f) The large scintillator above the lead shielding: This detector designed to record cosmic ray particles passing through the detector or the beamline during an event. No signal from this detector could be recorded. During the April to July 2018 shutdown a signal conversion problem (NIM/TTL) was identified and could be solved. The scintillator performed as expected during Run 3.

Meanwhile the detector has been removed from the experiment and is in Bonn.

2.) Data taking at the CDL

For the separation of signal (X-ray) from the background (tracks) we use a likelihood, which is based on three geometrical parameters of the event: Eccentricity, length divided by root mean square (rms) along the short axis and fraction of pixels within radius of one rms. These three event shape variables change their mean value and width in dependence of the energy for X-ray photons. To have a clean sample of signals with different energies, the detector was transferred to the CDL and mounted at the X-ray generator. By carefully selecting the initial beam energy, target material and filter material, one can generate 8 different photon energy lines between 277 eV and 8 keV. This setup is ideal to test and calibrate our detector and we have been taking data from February 15th to 19th 2019.
The data has been analyzed with respect to the energy calibration. Two example spectra are shown in figures 1 and 2, where the K_α-line of carbon (277 eV) and the K_α-line of copper (8.048 keV) are shown.

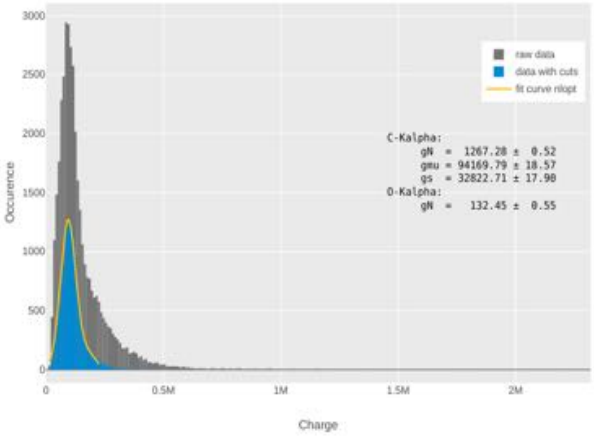

Figure 4: Kalpha-line of carbon with contamination of Kalpha-line of oxygen.

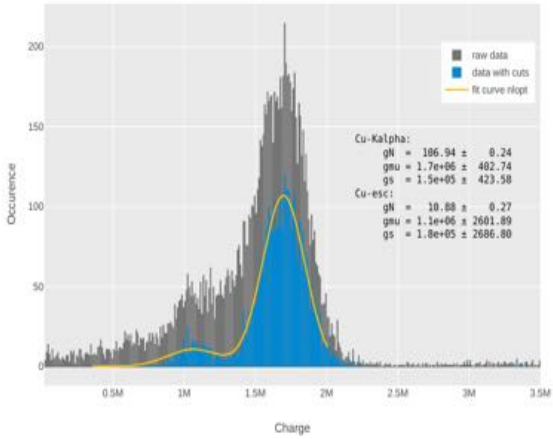

Figure 5: Kalpha-line of copper with argon escape line.

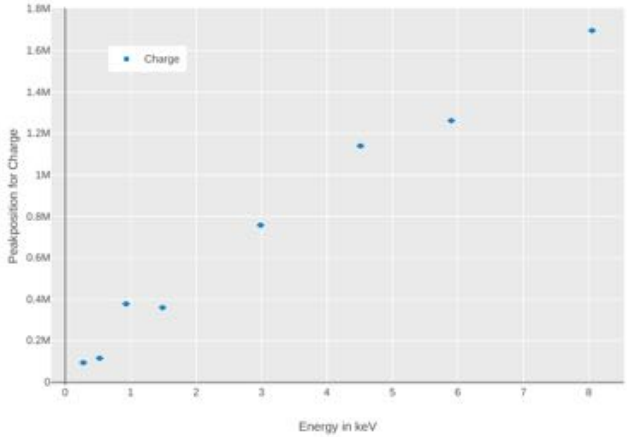

Figure 6: Calibration curve of the charge measurement

Determining the position of the line in the charge spectrum gives a measurement for the calibration curve shown in figure 3, which is important to determine the unknown photon energy of an event during data taking. Apart from the energy, also the important event shape variables have been studied and prepared for the input of the analysis code.
As examples, the eccentricity of photon events from a K-line of Mn is compared to a track-like background in figure 4. Since the variable is energy dependent, the distribution of a K_α-line of Mn is compared to the K_α-line of oxygen. Taking into account the differences in these distributions is important for the analysis.

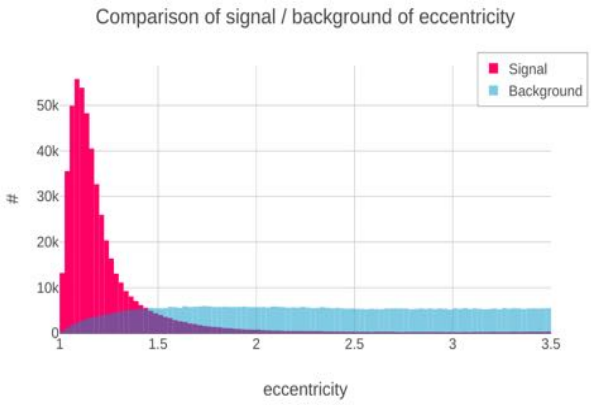

Figure 8: Comparison of the eccentricity of photons from the K_α-line of Mn (5.8 keV, blue) and track like background.

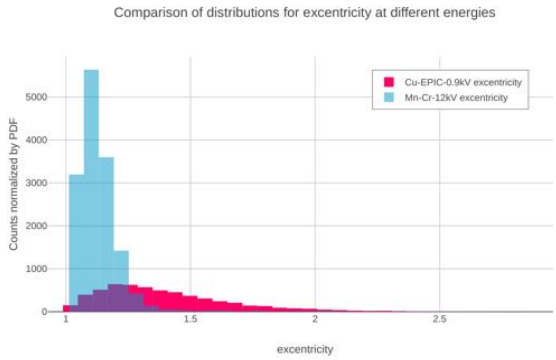

Figure 7: Comparison of the eccentricity of photons from the K_α-line of Mn (5.8 keV, blue) and oxygen (525 eV, red).

3.) Analysis of the 2014/2015 data: search for solar chameleons

The paper has been published by the Journal of Cosmology and Astroparticle Physics with the signature 01(2019)032 on January 16th 2019.

4.) Analysis of the 2017/2018 data

Because of the significantly increased amount of data per event (due to increasing the number of chips from one to seven) and the additional information available (FADC and veto signals), it was decided to rewrite the analysis framework in order to simplify the handling of the additional data. The code has been written including the additional functionality for the FADC, 7-chip readout and veto triggers. As a first check we are analyzing the 2014/2015 data with the new code and comparing the results with the published ones. Unfortunately, we observe some differences in the low energy region (below 2 keV), where the new code gives significantly lower results. This deviation is still under investigation.

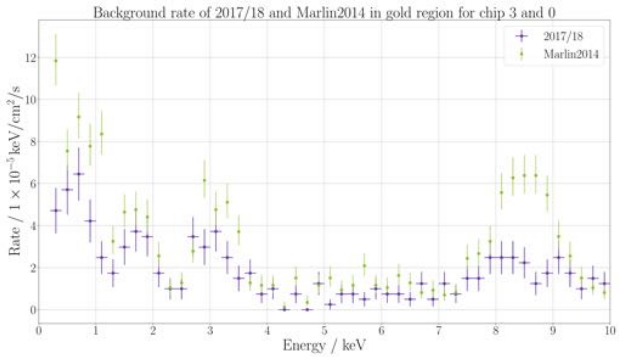

Figure 10: Comparison of background rate for gold region of old analysis of 2014/5 data and new analysis of Run-2.

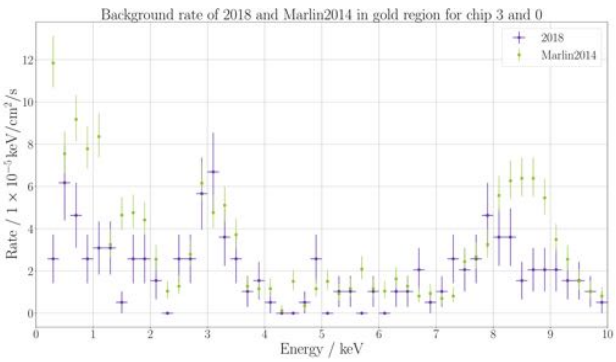

Figure 9: Comparison of background rate for gold region of old analysis of 2014/5 data and new analysis of Run-3.

Applying the new code to the data of the central GridPix detector of Run 2 and Run 3 gives similar spectra as the ones published with the 2014/2015 data (s. figures 6 and 7, still made with old CDL data). The only significant differences are in the low energy region as mentioned before and in the region between 8 and 9 keV. The latter region is dominated by the K_α-line of Cu (8.048 keV) and cosmic rays arriving vertically on the GridPix. As the 2017/18 setup had a much better lead shielding, a large part of the cosmic rays was stopped and did not reach the detector. This could explain the reduced count rate between 8 and 9 keV.

The impact of the additional features of the improved detector are still under investigation, but first properties can be presented.

a) **6-veto GridPixes:** The surrounding GridPixes are introduced as veto detectors. In case of a signal on the central GridPix, the surrounding GridPixes should show no signal. In figure 8 the number of hits on the surrounding detectors is shown. We have implemented an algorithm, which takes the distance of the signal from the central signal to the outer signal into account and judges, if they are correlated or random. Figure 9 shows an event where there is a round signal on the central GridPix, which is clearly connected to a track on the lower GridPix.

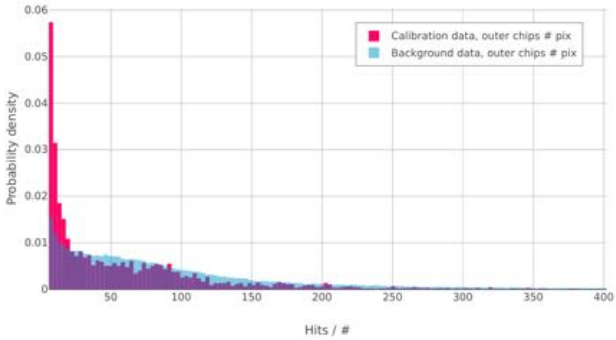

Figure 11: Number of pixels hit on the outer 6 GridPixes, when there is a photon-like event on the central ASIC

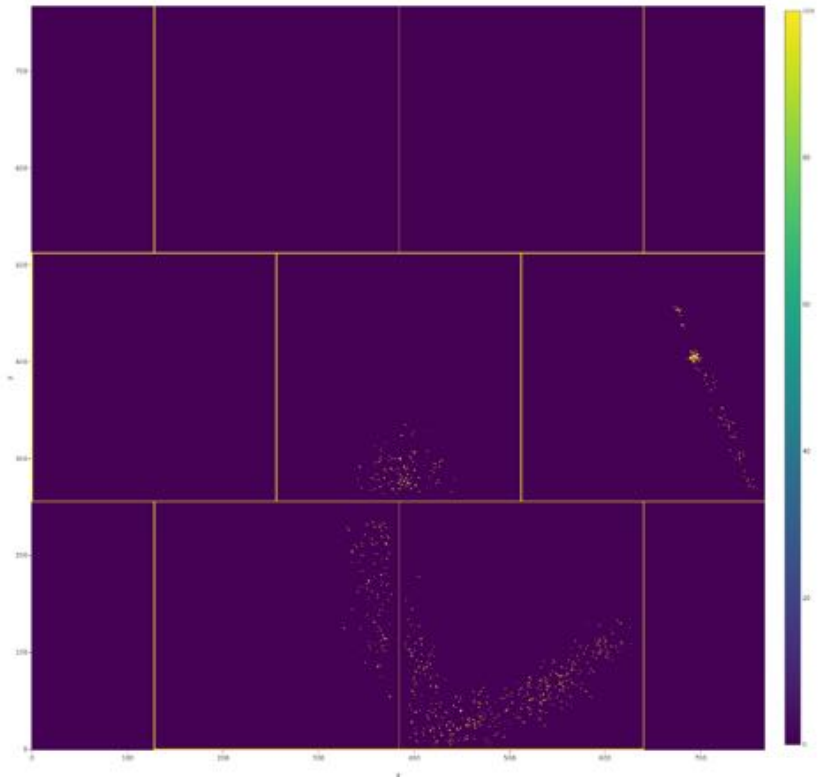

Figure 12: Event with tracks on the surrounding GridPixes.

b) FADC: The spectra of the rise time of the signal as recorded by the FADC is shown in figure 10. Taken with a 100 ns shaping time during Run 3, the clear difference between the two distributions of X-ray photons from the ^{55}Fe source and background tracks. This can be used with either a cut or later as a possible input of a likelihood method to separate signal from background.

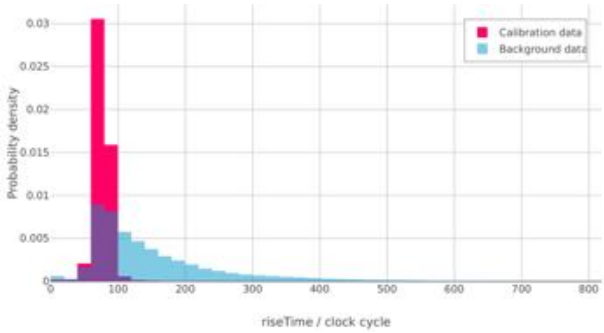

Figure 13: Distribution of rise time for ^{55}Fe and background data taking.

c) veto signals: The time distribution of the scintillator signal and the arrival time of the signal on the grid recorded by the FADC is shown in figures 11 and 12.

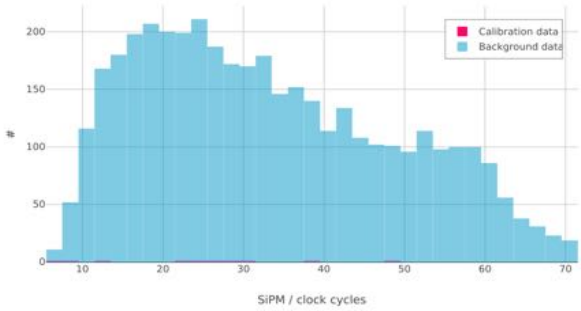

Figure 14: Time distribution between signal of SiPM scintillator and FADC signal.

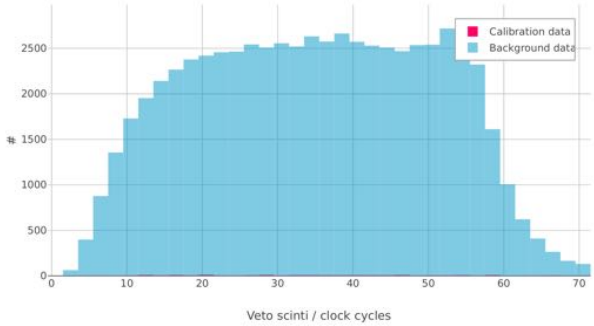

Figure 15: Time distribution between signal of large scintillator and FADC signal.

The different distribution results from the different orientation of the particles: Particles passing through the small scintillator are mostly horizontal and pass also directly through the grid resulting in a fast rise of the distribution and a maximum at a low number of clock cycles. In contrast particles passing through the large veto scintillator follow a vertical pass generating a track parallel to the grid. This gives an equally distributed signal and a sharp fall, when of the distribution when the particles have to pass through the cathode.
The signal can be used to veto events with a cosmic ray, which could look like an X-ray photon or could have generated a fluorescence photon.

d) Implementation of additional features in the analysis: Though several details still have to be studied a first, cut-based implementation of the vetoes based on the new detector features has been implemented. The cuts are only rough estimates at the moment and have not been optimized yet. In the figures 13-15 we see the effect of the different cuts on the remaining background spectrum in the gold region, i.e. in the ~1 cm² central area of the central GridPix, where the axion image of the Sun is expected. In all cases the rate is reduced in different energy ranges as expected. The rate reduction is significantly higher in the area outside the gold region, where also more background is observed.

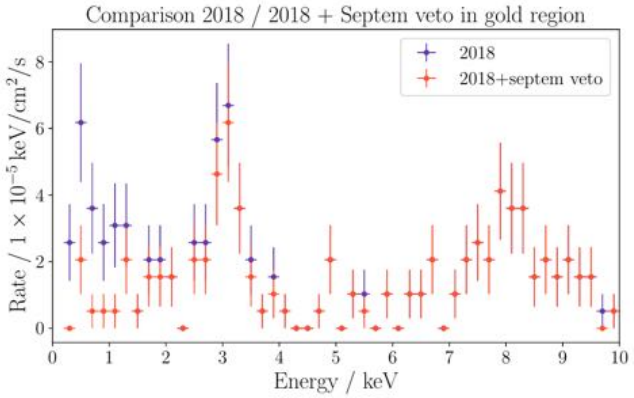

Figure 16: Comparison of background rate in gold region with and without taking into account the signal on the surrounding GridPixes.

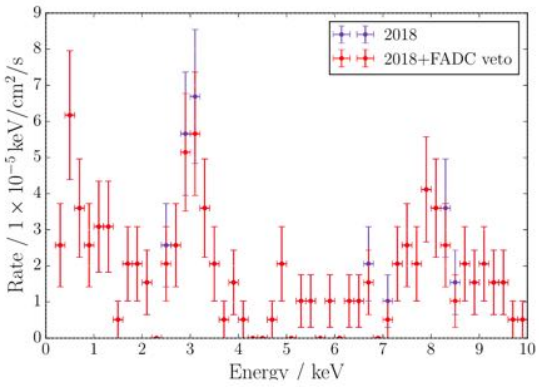

Figure 17: Comparison of the background rate in the gold region with and without taking the risetime of the FADC into account.

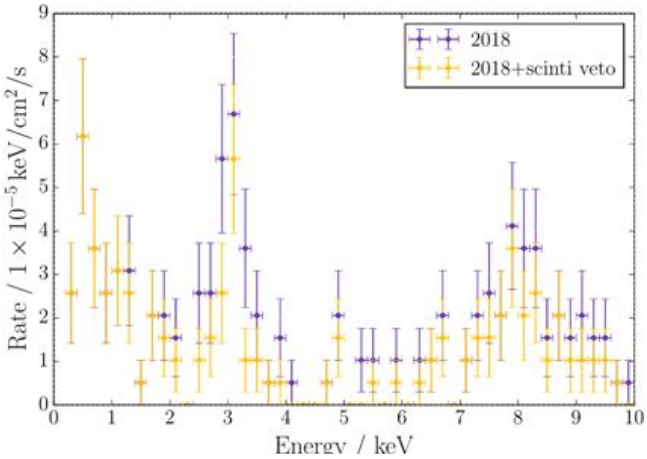

Figure 18: Comparison of background rate in the gold area with and without considering the signals of the veto scintillators.

5.) Ray tracer simulation of axions

To improve the understanding of axion production in the Sun and losses on the way to the conversion point, we have worked on the implementation of a ray tracer to simulate the expected flux of axions from the Sun and resulting flux of X-rays after conversion in the CAST magnet. It takes into account the properties of the LLNL X-ray telescope as for example the shell structure, which can be clearly seen in figure 16, which is a zoom in of the axion image and only a small part of the central GridPix.

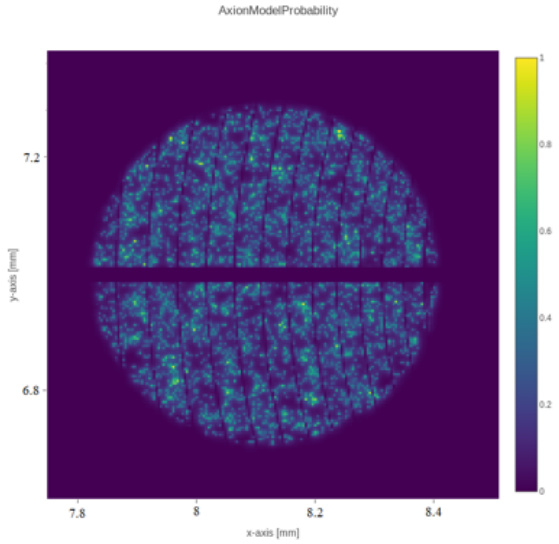

Figure 19: Axion image as seen through CAST including the LLNL telescope.

KWISP solar chameleon detector

Working group: J. Baier, G. Cantatore, S. Cetin, H.Fischer, A. Gardikiotis, M. Karuza, Y. Semertzidis, M. Vretenar, K.Zioutas

Introduction

The KWISP ultra-sensitive optomechanical sensor is searching for chameleons at CAST by detecting the force exerted on a micro-membrane by a solar chameleon beam reflecting off it. KWISP exploits both the focusing action of the ABRIXAS telescope, and the sun-tracking capability of the CAST magnet. Several versions of the detector have been built, tested and used for solar tracking data runs in a continuous upgrade effort aimed at reaching the ultimate shot-noise limited sensitivity.
In the following sections we will briefly discuss the recently published results obtained with the first version of KWISP, dubbed "version 1.5", the status of the latest version, KWISP 3.0, a few preliminary results obtained with KWISP 3.0, and the proposed future developments of this original technique.

Results from KWISP Version 1.5

In KWISP 1.5, membrane displacements are read out with a Michelson-type interferometer, where the membrane plays the role of a mirror in one of the two interferometer arms. In order to enable detection, the expected chameleon beam is amplitude modulated at a known frequency (984 Hz) with a mechanical "chameleon chopper". The recently published results [1] come from a data taking campaign conducted in 2017 with the detector mounted on the CAST magnet and tracking the sun. A minimum detectable force limit of 80 pN at 95% confidence level was reached, allowing us to set original bounds in the chameleon parameter space β_γ-β_m (photon coupling – matter coupling). In this article, an effort is made to calculate the force on the membrane resulting from the expected solar chameleon flux, including the shielding effects of the CAST infrastructure. In addition, the response of the membrane to a given force, resulting in an "equivalent spring constant" of (1200±400) N/m, was determined in a series of separate measurements. These findings also apply to the performance of later versions of KWISP. Version 1.5 is now used for calibrations and to test custom membranes and other ideas.
Figure 1 below shows the schematic layout of KWISP 1.5. The 5x5 mm^2, 50 nm thick, Si_3N_4 membrane acts as one of the mirrors in a Michelson interferometer, and its movements, possibly caused by the force exerted by a solar Chameleon beam, result in displacements of the interferometer interference fringes.

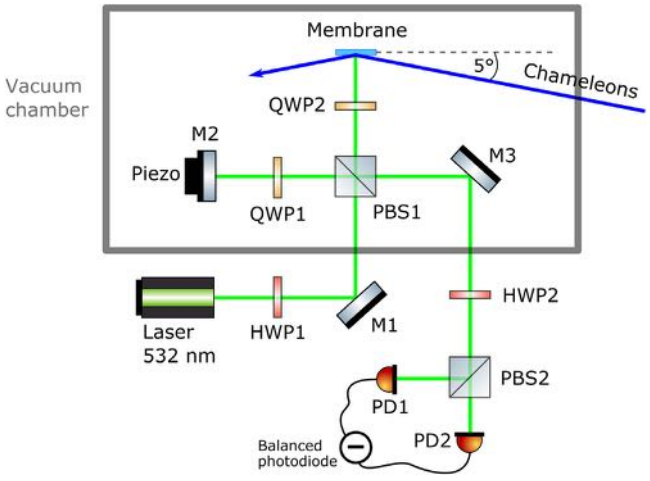

Figure 1 – Schematic optical layout of the KWISP 1.5 detector. The detector is mounted on the CAST magnet in such a way that the expected solar chameleon beam, focused by the ABRIXAS telescope, impinges on the membrane at a 5° grazing incidence angle.

The flux of chameleons leaving the sun and streaming to Earth was calculated under the assumption that production takes place in the sun tachocline region through the Sikivie effect caused by the local magnetic fields. Following the literature, we took a tachocline thickness between 1% and 5% of the solar radius R_{Sun}, and the magnetic field intensity between 10 T and 30 T. The results of this calculation are given in Figure 2. To determine the force expected on the membrane due to the solar chameleon beam, one must first take into account the shielding effects due to atmosphere and to the CAST infrastructure. Figure 3 shows the chameleon energy range actually accessible to the detector. This range is then used to obtain the plots of Figure 4, which give, for three different sets of parameters in the chameleon interaction potential, the expected chameleon force on the KWISP membrane as a function of the matter coupling β_m. In the figure, the orange band represents the 95% confidence level interval centered around the average minimum force of (44±18) pN detected during sun-tracking runs.

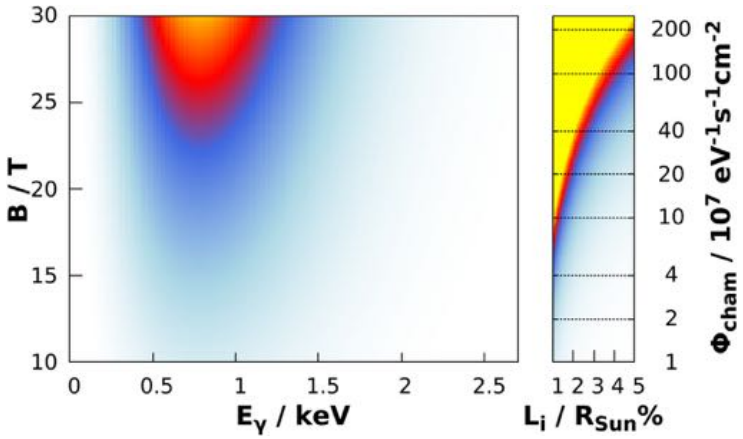

Figure 2 – Calculated chameleon flux leaving the sun for a tachocline thickness 1-5% of R_{Sun}, and a 10-30 T magnetic field (see also text). The graphs can be read as follows. For a chosen chameleon energy and tachocline magnetic field intensity pair, a color code is found in the leftmost graph. This color then identifies a band in the rightmost graph giving the chameleon flux as a function of tachocline thickness (L_i) measured as a fraction of R_{Sun}.

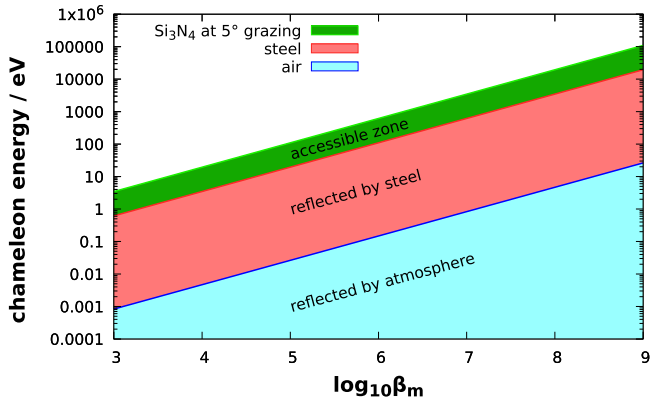

Figure 3 – Chameleon energy range accessible to KWISP 1.5. Only chameleons with masses falling within the green band in the figure contribute to the total pressure on the membrane (see also text).

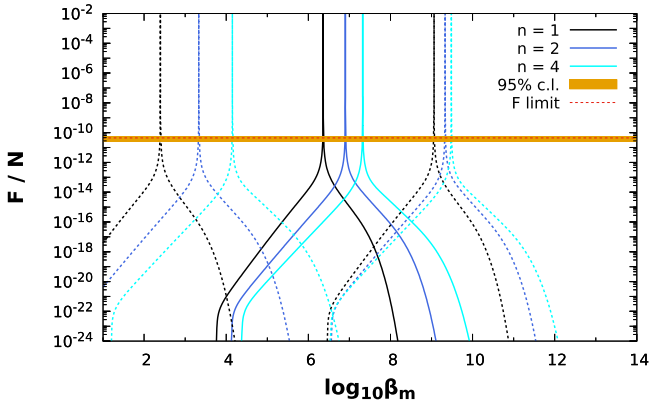

Figure 4 – Expected chameleon force on the membrane calculated for a tachocline thickness of 5%·R_{Sun}. Solid lines correspond to a dark energy scale of 2.4 meV, dashed lines to 10^{-5} eV, and dotted lines to 0.1 eV. The orange band represents the 80 pN, 95% confidence level, interval of the minimum detected force (see also text).

Finally, from the KWISP 1.5 measurements we obtained the constraints on solar chameleons in the β_γ-β_m (photon coupling – matter coupling) plane detailed in Figure 5 below. Here the overall CAST bounds (GridPix+KWISP) are shaded in red. Results from other experimental tests are also reported, shaded in blue, along with the recent claim [2] by experiments based on atom interferometry. The results of the latter are based on a purely virtual chameleon exchange, as opposed to real chameleon interactions with the KWISP membrane, while "GammeV-CHASE" results rely on two successive photon-chameleon and chameleon-photon conversions.

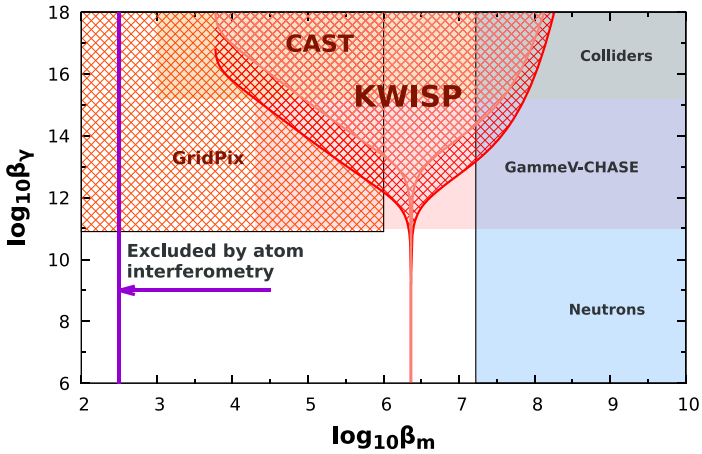

Figure 5 – Overall CAST bounds on solar chameleon coupling strengths combining GridPix and KWISP 1.5 results (shaded in red). KWISP ounds are calculated assuming a dark energy scale of 2.4 meV and a chameleon potential index n = 1. The uppermost curve corresponds to a 10 T field and L_i = 1%·R_{Sun}, while the lower curve to a 30 T field and L_i = 5%·R_{Sun}. Other experimental results are included for comparison purposes (see text).

Status of KWISP Version 3.0

The latest incarnation of the detector, KWISP version 3.0, is now mounted on the CAST beamline behind the ABRIXAS telescope, and is presently taking physics data. The sensing of membrane displacements is here accomplished by a Fabry-Perot (FP) interferometer in a "membrane-in-the-middle" configuration [3].

The main characteristics of KWISP 3.0 are complete fiber-optic beam transport, single-piece monolithic aluminum base, miniaturized optics and full passive vibration isolation. This last feature

allows continuous operation of the sensor in the FP cavity locked state also with vacuum pumping on, which was not possible with previous versions. The detector consists of two parts, an "injection bench" housing the main laser and sitting on the experimental hall floor, and a "detection bench" mounted on the CAST magnet. The two benches are connected by a 40 m-long optical fiber.
In order to better control mechanical vibrations affecting the performance of the detector and to bring all the critical optics, especially the Fabry-Perot cavity and its matching optics, on a single platform, the optics layout of the detection bench was completely redesigned with respect to previous versions, and it now fits on a monolithic Al baseplate located inside the vacuum chamber and vibrationally isolated by means of special passive feet, visible in Figure 6. A schematic layout of KWISP 3.0, is drawn in Figure 7. The amplitude modulation of the incoming chameleon beam is now accomplished by a Texas Instrument DLP LightCrafter 9000 chip consisting of about 4 million micro-mirrors with a pitch of 7.6 μm, which can be synchronously tilted, thus providing chopping action on the beam at a chosen frequency of about 2.5 kHz. Details of the chopper and its control electronics are visible in Figure 8, while the image in Figure 9 shows the chopper in position between the ABRIXAS telescope (on the left) and the detector vacuum chamber (at right).

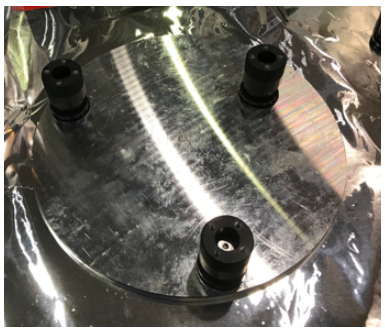

Figure 6 – Detail of the vibration isolation feet supporting the KWISP 3.0 baseplate.

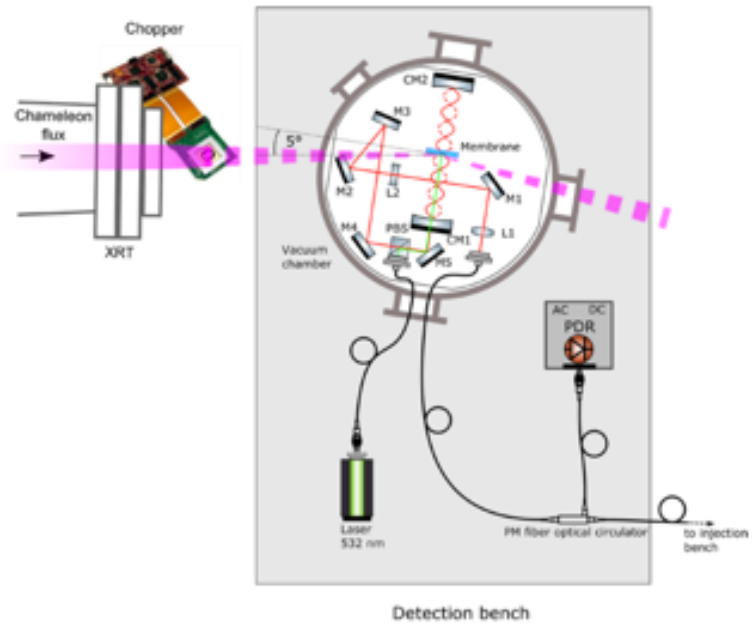

Figure 7 – Schematic layout of KWISP 3.0. All the optical elements are fixed on a single monolithic aluminum base fitting inside the vacuum chamber. Mirrors and lenses are mounted on high-quality manually-actuated mounts and the base rests on three passive vibration isolation feet (Mod. VIB100-0512 by Newport) to completely decouple the optics from the chamber and the rest of the apparatus. The 1064 nm measuring laser beam is transported into the vacuum and injected into the optical system using an optical fiber. A second fiber transports a 532 nm auxiliary beam which can be used for alignment and for calibration of the membrane sensitivity with radiation pressure. A DLP chip is used to amplitude modulate the chameleon beam at a chosen frequency of 2370 Hz (see also text).

A top view of the detection bench with the baseplate secured alongside the vacuum chamber for preliminary alignment is visible in Figure 10.
Figures 11 and 12 show the injection bench, and a close-up picture of the Fabry-Perot cavity with the membrane at its center, respectively. Figure 13 presents a top view of the vacuum chamber with the fully assembled opto-mechanical sensor positioned inside and ready to be closed for pumping, while the detection bench in the final running condition, after proper alignment with the DLP chameleon chopper and the incoming chameleon beam, is presented in Figure 14.

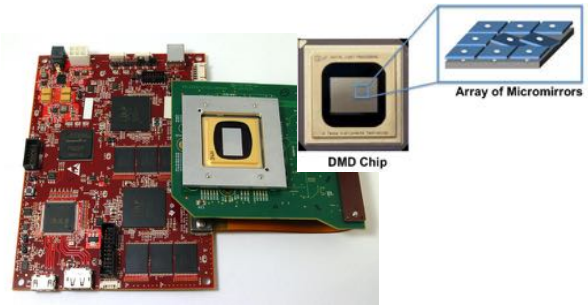

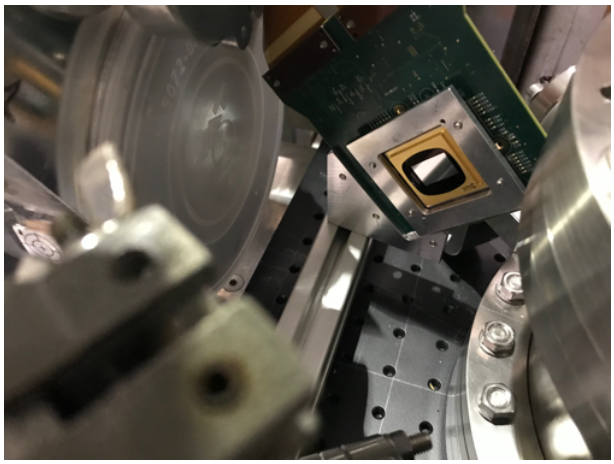

Figure 8 (left) – Illustration of the Texas Instrument LightCrafter 9000 DLP chip with its control board. The insert at upper right shows a detail of the geometry of the micro-mirrors.
Figure 9 (right) – The DLP chip used as a chameleon chopper aligned to intercept the expected solar chameleon beam (impinging from the left), and direct it towards the KWISP 3.0 membrane (not visible, at right inside the vacuum chamber).

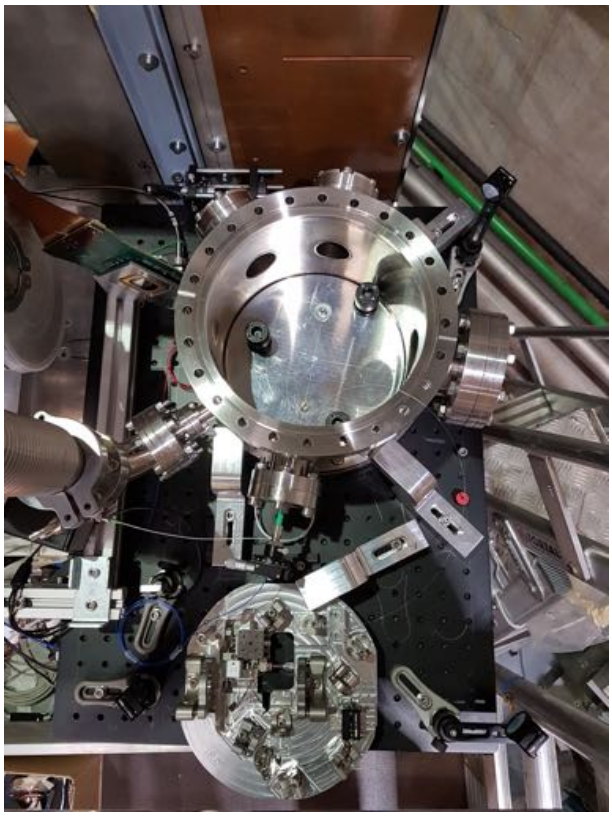

Figure 10 – Top-down view of the detection bench with the detector baseplate extracted from the vacuum chamber and positioned alongside it for the alignment procedure. Notice the vibration isolation feet fixed inside the vacuum chamber.

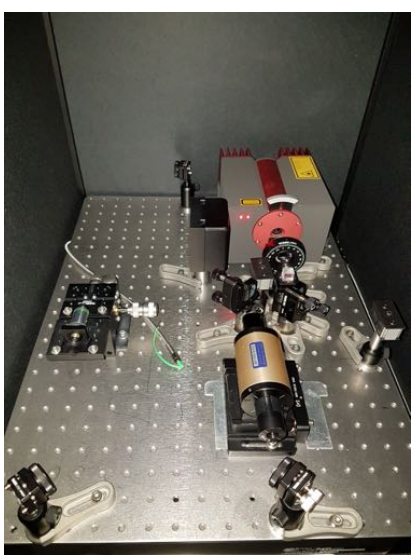

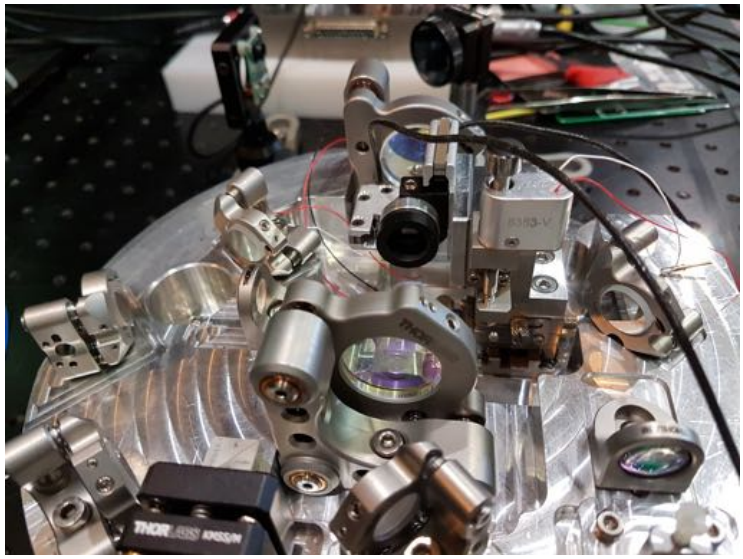

Figure 11 (left) - View of the injection bench. The picture shows the inside of the safety enclosure housing the laser (upper right), beam conditioning optics, and the fiber-launch system (center left).
Figure 12 (right) – Close-up photograph of the KWISP 3.0 baseplate showing a view along the Fabry-Perot cavity axis. The membrane is visible inside its holder (black cylinder) at the center of the picture, placed between the two cavity mirrors (foreground and background).

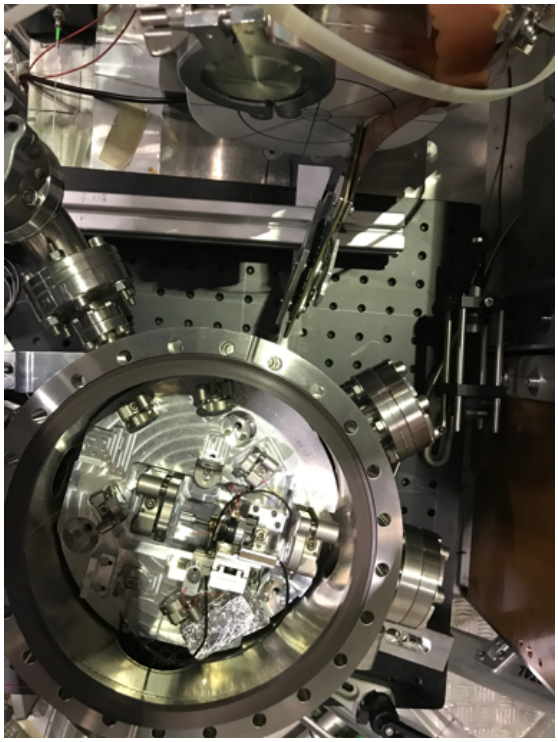

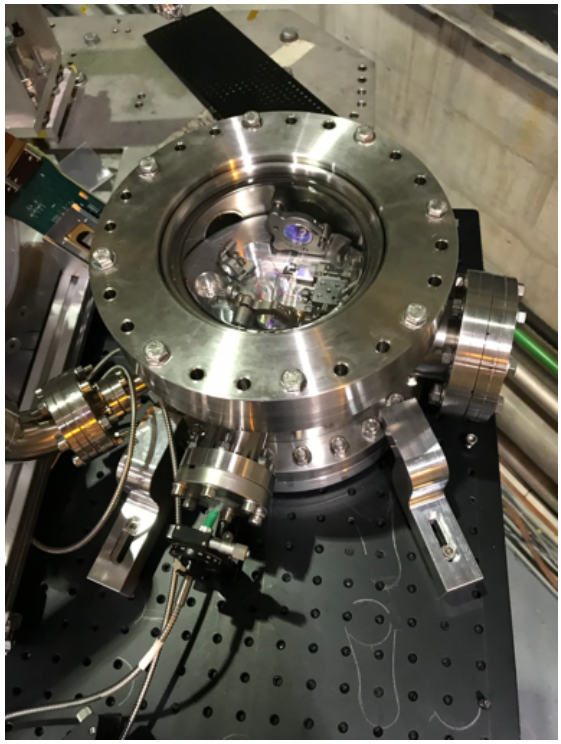

Figure 13 (left) - View of the fully assembled KWISP 3.0 optomechanical sensor positioned inside its vacuum chamber and ready for pumping
Figure 14 (right) – KWISP 3.0 detection bench under vacuum and in running condition. The sensor itself is visible through the window on top of the vacuum chamber, and the optical fiber transporting laser light to the sensor is in the foreground. In this picture, the expected chameleon beam comes from the left.

Recall that the signal containing the information on membrane displacements is the “error signal” of the feedback loop which keeps the laser tuned at resonance with the Fabry-Perot interferometer. This signal is generated by the feedback amplifier circuit used to sense the instantaneous difference in frequency between laser and cavity, and to provide a correction voltage subsequently applied to the laser tuning input to keep it at resonance. Figures 15 and 16 show oscilloscope screenshots with examples of such signals in the unlocked and in the locked state, respectively. In Figure 15, the blue

trace represents the error signal, the light blue trace the correction voltage, and the magenta trace is the intensity of the light reflected back from the cavity. In the unlocked state the correction voltage is an externally applied sawtooth signal that causes the laser frequency to sweep up and down a few 10's of MHz. When the laser frequency crosses the cavity frequency resonance occurs and light enters the cavity: this "missing" light appears as a negative peak in the magenta curve. Correspondingly, an error signal also appears in the blue curve. When in the locked state, the slope of the latter is used by the circuit to control the correction signal and hence the laser frequency. Figure 16 shows the same signals of Figure 15, but with the system under lock. In this state both error and correction signal stay near zero volts, and the reflected light intensity assumes a constant value lower than that in the unlocked state, signifying that light is actually being accumulated in the cavity.

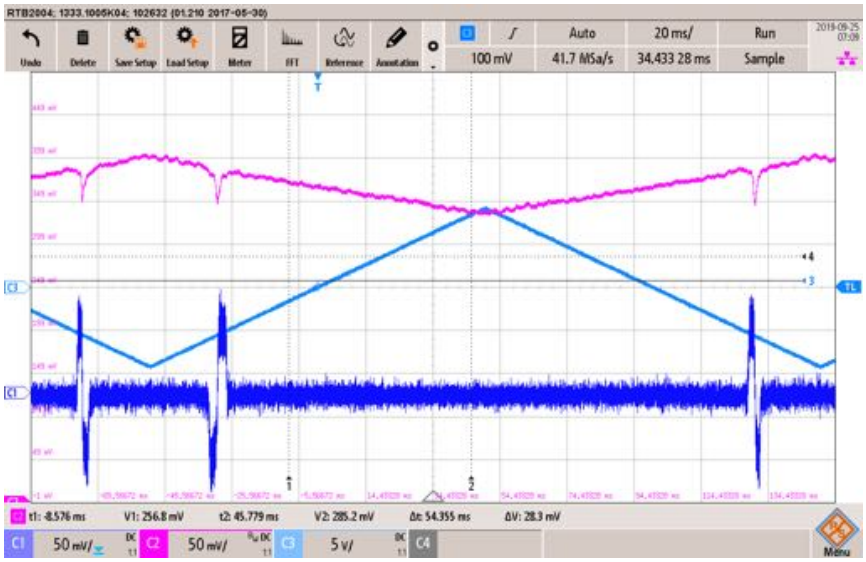

Figure 15 – Laser frequency feedback loop control signals in the unlocked state (see text). Blue – error signal. Light blue – laser frequency control voltage. Magenta – reflected light intensity.

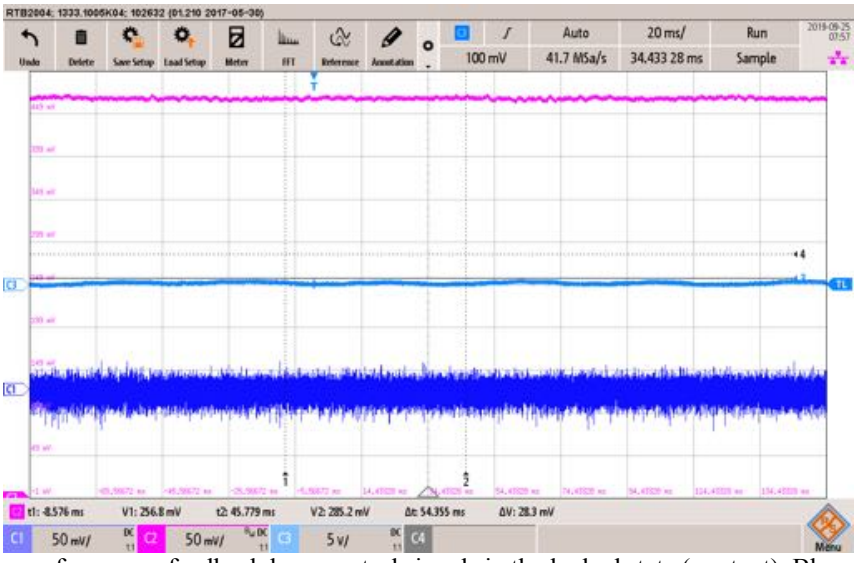

Figure 16 – Laser frequency feedback loop control signals in the locked state (see text). Blue – error signal. Light blue – laser frequency control voltage. Magenta – reflected light intensity.

In KWISP 3.0 the locked state is stable and can be maintained also when pumping on the vacuum chamber. This was not possible with previous versions of the sensor, and it actually contributes towards reducing the noise, as the membrane is not subject to spurious forces due to pressure gradients when the base pressure (~10^{-5} mbar) is kept stable by pumping. One way to check the proper operation of the sensor is to acquire a wideband spectrum of the error signal and to observe the presence of a

peak at the membrane mechanical resonant frequency due to the thermally excited motion of the membrane itself. In the spectrum plotted in Figure 17 the membrane "thermal" peak is clearly visible at 82.5 kHz, which is the fundamental mechanical resonance frequency of our membrane (5x5 mm^2, 50 nm thick, Si_3N_4, the same as KWISP 1.5). The other narrower peaks are spurious and are due to environmental disturbances in the CAST area. The shape of the noise floor is also due to the environmental conditions. The noise level at the base of the "thermal" peak of Figure 17 corresponds to a membrane displacement of $8.0 \cdot 10^{-15}$ m or, using the same equivalent spring elastic constant given above for KWISP 1.5, a force level of 10 pN. The spectrum was taken with the CAST magnet stationary in parking position and with the chopper off.

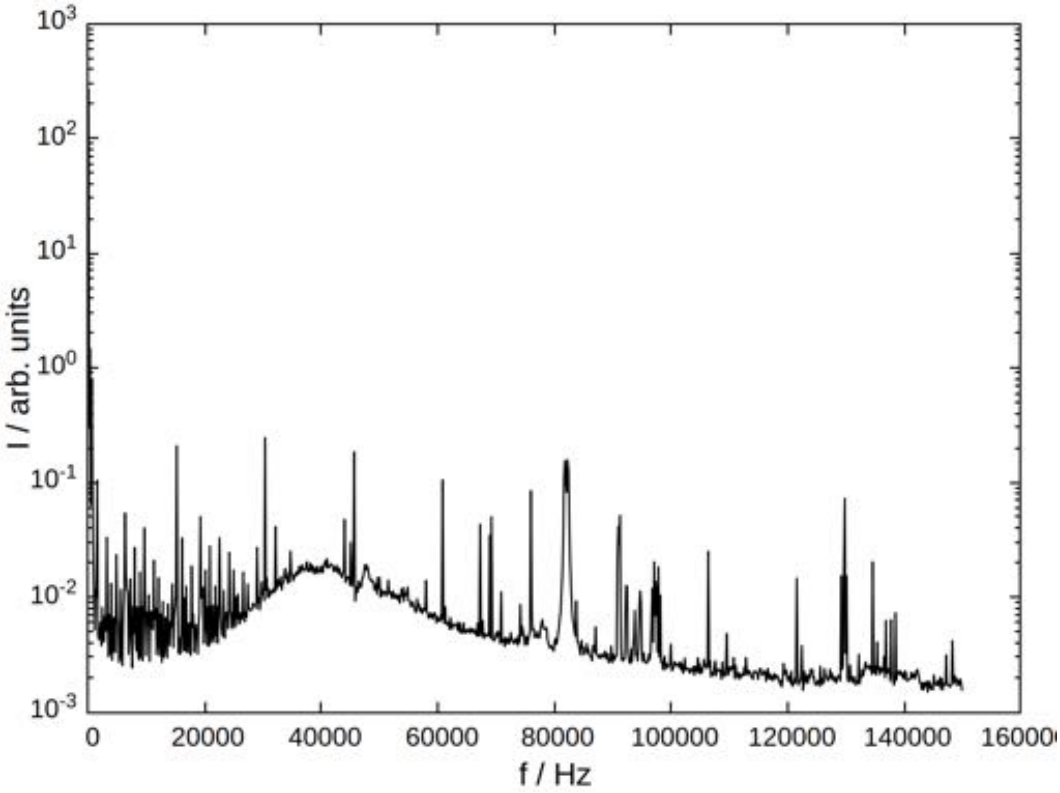

Figure 17 – Wideband test spectrum of the feedback loop error signal taken with the CAST magnet in parking position and the chopper off. Integration time was 34 s. Note the wide membrane "thermal peak" at 82.5 kHz. The noise floor around this peak corresponds to a displacement of $8.0 \cdot 10^{-15}$ m, or to a force of 10 pN (see also text).

Thanks to the presence of the chopper, the frequency at which a possible chameleon signature should appear is known, and can be adjusted within the 0-10 kHz range of the DLP chip to fall in a low noise frequency region. In order to exclude the possibility that a spurious signal is induced by the chopper itself, we conducted a series of background studies to compare the "chopper on" and "chopper off" configurations. Figure 18 shows a spectrum of the error signal around the chosen chopper frequency (2370 Hz in this case) when the chopper chip is powered but not excited ("off" state, micro-mirrors not moving). Figure 19 shows a spectrum taken in similar conditions but with the chopper in the "on" state (micromirrors moving). Note that no peak at 2370 Hz is visible in both cases.

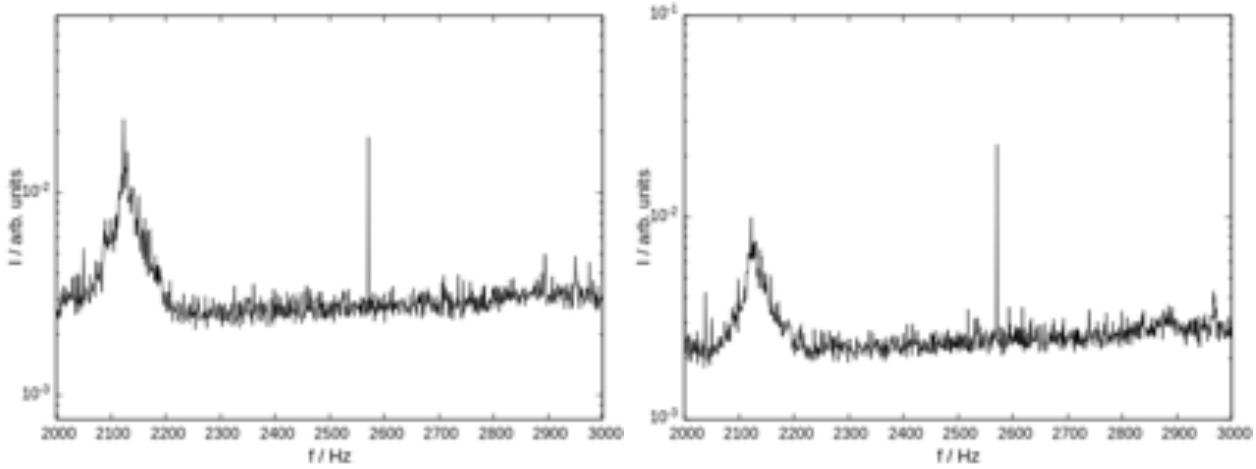

Figure 18 (left) – Spectrum of the error signal around the chopper frequency (set at 2370 Hz) with the chopper "off". The narrow peak at ~2570 Hz is spurious (see also text).
Figure 19 (right) – Spectrum of the error signal around the chopper frequency (set at 2370 Hz) with the chopper "on". Note that no peak is visible at the chopper frequency. The narrow peak at ~2570 Hz is spurious (see also text).

Preliminary results

KWISP 3.0 is presently taking physics data during the morning sun tracking runs at CAST. In a typical data taking sequence several ~10 minutes-length data sets ("slow") are recorded at a small bandwidth setting to resolve the frequency region around the chopper frequency (2370 Hz). At the beginning of data taking, and after each 10-minute record, a short 34 s record ("fast") is taken at a wide bandwidth setting in order to check the presence of the membrane thermal peak. Normally, in a tracking session 4 "slow" sets are taken for a total of ~2300 s of data.
The current KWISP 3.0 sensitivity during sun tracking is about $5 \cdot 10^{-14}$ m/√Hz, allowing us to reach a force limit of 2.4 pN in just 554 s of integration time, a factor ~20 better than the published bound achieved with KWISP 1.5.
The data taking campaign at CAST is still ongoing, and at the time of writing we have accumulated about 20500 s of tracking data. Examples of spectra extracted from "fast" and "slow" records acquired during sun tracking are plotted in Figure 20 and Figure 21.

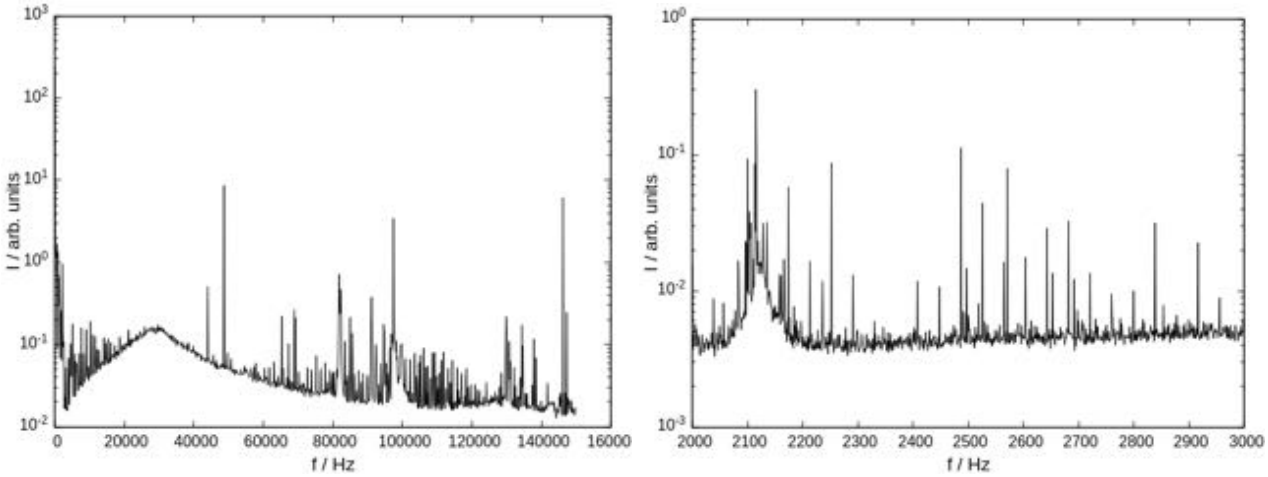

Figure 20 (left) – "Fast" spectrum of the error signal during sun-tracking. Note the membrane thermal peak at 82.5 kHz (see text)
Figure 21 (right) – "Slow" spectrum of the error signal during tracking. No peak is visible at the chopper frequency of 2370 Hz (see text)

Using the data collected so far, we can present here some preliminary results in terms of chameleon parameters. No peak is visible in the data at the chopper frequency, thus we proceed to set bounds on chameleon interaction strength. Figure 22, taken from [1], shows a plot of the force expected on the membrane by a solar chameleon beam for different values of the constants in the chameleon interaction potential. The yellow band in the plot represents the minimum force level detectable with KWISP 1.5, while the horizontal black line represents the minimum force level already detectable with KWISP 3.0. Both levels are determined after taking into account the shielding due to the CAST infrastructure.

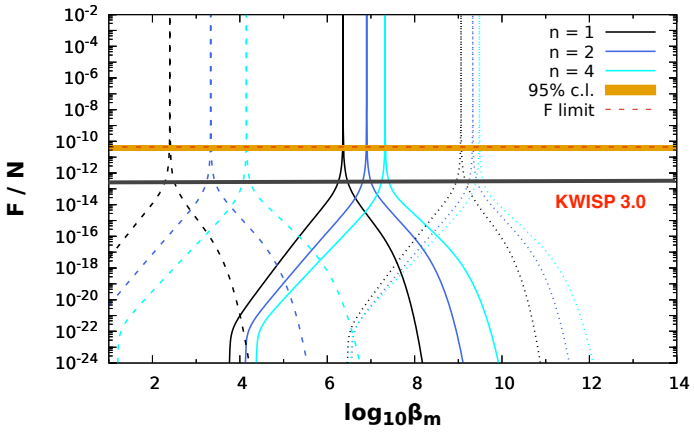

Figure 22 - Expected force at the sensor membrane (taken from [1]). Different line styles correspond to different choices of dark energy scale in the chameleon potential: solid $\Lambda = 2.4 \cdot 10^{-3}$ eV, dashed $\Lambda = 1 \cdot 10^{-5}$ eV, and dotted $\Lambda = 0.1$ eV. The orange band represents a 95% confidence interval centered at the minimum average force level detectable with KWISP 1.5. The horizontal black line represents the minimum force level presently detectable with KWISP 3.0 (see text).

Correspondingly, Figure 23, also taken from [1], shows a plot of the exclusion region in the β_γ–β_m plane reachable with the current KWISP 3.0 dataset. Exclusion regions obtained with different techniques are also reported for comparison.

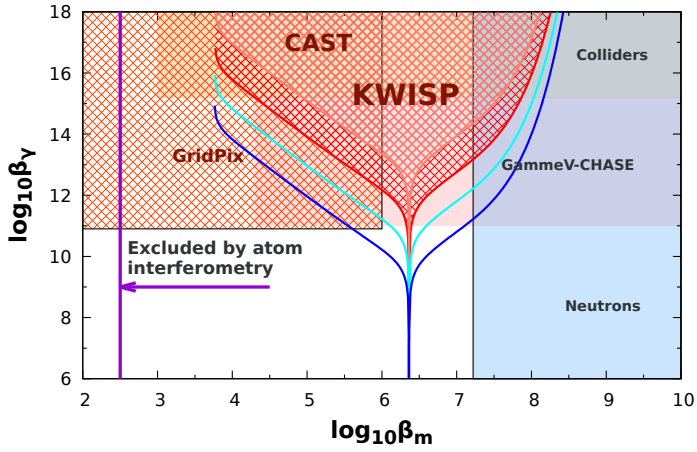

Figure 23 – Preliminary exclusion regions in the chameleon parameter space already obtained at CAST by KWISP 3.0 with 554 s (light blue line) and 20500 s (dark blue line) of integration time. The red hatched pattern marks existing CAST bounds taken from [1]. The KWISP exclusion zones are calculated assuming a dark energy scale $\Lambda = 2.4 \cdot 10^{-3}$ eV and n = 1. The limit from the previous CAST measurement (GridPix) is based on chameleon-to-photon conversion only [4]. Areas explored by other experiments [5, 6, 7], including atom interferometry [8], which claims to exclude all $\beta_m \geq 10^2$, are based on purely virtual chameleon exchange and on "afterglow" experiments, which rely on two successive photon-chameleon and chameleon-photon conversions. The KWISP measurements are directly sensitive to real chameleon interactions and are therefore complementary to other existing bounds.

Proposed improvements and upgrades, perspectives with KWISP 3.0

KWISP 3.0 main aim is to achieve shot-noise limited operation at room temperature. For example, with 150 μW of light power input into the cavity, which is about the currently employed level, this would correspond to a displacement sensitivity of $7.0 \cdot 10^{-16}$ m/√Hz, a factor ~100 below the current value.
Towards this goal, a series of short- and medium-term improvements is planned for KWISP 3.0.

Timescale of 1 month:

- install vacuum electrical feedthroughs to:
  - remotely control membrane alignment
  - remotely displace the membrane along the cavity axis in order to find a more sensitive position
- substitute the current ferrule-tipped input fiber with a fiber tipped with an FC/APC connector or with an input fiber with AR coating

The membrane longitudinal position along the cavity axis influences the sensitivity since it might be in a place where the slope of the "detuning curve" is flat, and the system is therefore less responsive to membrane displacements (for an explanation and an example of a "detuning curve" see [3]).
The use of an input fiber with a different tip will reduce noise in the light reflected back from the cavity.

Timescale of 2-3 months:

- improve detector calibration
  - re-measure the detuning curve
  - redesign the optics layout to implement direct calibration with a 532 nm auxiliary laser beam
- implement homodyne readout of the force sensor (see for instance [9])
- modify sensor mechanics to extend the data taking range during sun-tracking
  - shrink the diameter of the monolithic Al bench (requires redesign of the optics)
  - sandwich the Al bench between top and bottom vibration isolation feet (requires mechanical redesign)

In addition to lowering the noise background, a gain in sensitivity to a signal can be expected by matching the chopper frequency to the membrane mechanical resonant frequency. In this case, the amplitude of membrane displacements in response to a given force will be amplified by the mechanical quality factor Q of the membrane, and a sufficiently strong signal will appear superimposed on the "thermal peak" of the membrane. We plan to pursue this matching by acquiring choppers, now becoming available, capable of operating at maximum frequencies near 40 kHz. This will increase the current upper chopper frequency limit (~10 kHz) by a factor 4. In parallel, we are conducting studies to lower the membrane resonant frequency, presently at 82.5 kHz, to match the chopper frequency. This can be achieved, for instance, by coating a "bare" membrane with a thin layer (~ nm) of Au. A series of tests will be carried out on sample membranes specially coated for this purpose using KWISP 1.5 as a test bench.
A further gain in sensitivity for KWISP will come by operating the sensor at cryogenic temperatures. Once in the shot-noise limited regime, cooling the membrane has the effect of lowering the amplitude of the "thermal peak" and making a possible signal peak stand out more clearly, with a gain in signal-to-noise ratio. We foresee starting in 2020 a feasibility study for a Liquid-He cryostat to bring the system down to 4 Kelvin, thus lowering thermal effects by factor of 10, not too distant from the shot-noise floor. The challenge is to design and build a cryostat fitting on the CAST magnet and capable of housing a Fabry-Perot interferometer with the membrane in its middle. The monolithic aluminum base of KWISP 3.0 makes it ready to be integrated in a cryogenic cooling system designed to lower

the temperature of the membrane and other optical components. If preliminary studies are successful, and funding becomes available, cryostat construction and operation can begin in 2021. The ultimate goal would be to achieve milli-Kelvin temperatures by equipping the LHe cryostat with a dilution refrigerator stage, suppressing the thermal effects well below the shot-noise floor. In this regime the detector would be sensitive to attometer membrane displacements, comparable to the capability of present interferometric gravitational wave detectors. In this case, CAST would have the potential to improve by a factor ~100 its coverage depth in the chameleon parameter space.

References

[1] S. Arguedas Cuendis, J. Baier, K. Barth et al. [CAST Collaboration], Physics of the Dark Universe 26 (2019) 100367).
[2] D. O. Sabulsky, I. Dutta, E. A. Hinds, B. Elder, C. Burrage, and E. J. Copeland, Phys. Rev. Lett. **123**, 061102 (2019).
[3] M. Karuza, G. Cantatore, A. Gardikiotis, D. H. H. Hoffmann, Y. K. Semertzidis, and K. Zioutas, Physics of the Dark Universe **12**, 100 (2016).
[4] V. Anastassopoulos, et al. [CAST Collaboration], JCAP 01 (2019) 032. doi: doi.org/10.1088/1475-7516/2019/01/032.
[5] A. Upadhye, J. H. Steffen, A. Weltman, Phys. Rev. D 81 (2010) 015013. doi:doi.org/10.1103/PhysRevD.81.015013.
[6] J. H. Steffen, et al., Phys. Rev. Lett. 105 (2010) 261803. doi:doi.org/10.1103/PhysRevLett.105.261803.
[7] P. Brax, C. Burrage, A.-C. Davis, D. Seery, A. Weltman, Journal of High Energy Physics 2009 (09) (2009) 128–128. doi:10.1088/1126-6708/ 2009/09/128.
[8] D. O. Sabulsky, I. Dutta, E. A. Hinds, B. Elder, C. Burrage, and E. J. Copeland, Phys. Rev. Lett. 123, 061102 (2019).
[9] P. Piergentili, *Optical cooling of a mechanical micro-oscillator revealed by homodyne detection,* PhD Thesis, University of Camerino, Italy (2014).